



저작자표시-비영리-변경금지 2.0 대한민국

이용자는 아래의 조건을 따르는 경우에 한하여 자유롭게

- 이 저작물을 복제, 배포, 전송, 전시, 공연 및 방송할 수 있습니다.

다음과 같은 조건을 따라야 합니다:



저작자표시. 귀하는 원저작자를 표시하여야 합니다.



비영리. 귀하는 이 저작물을 영리 목적으로 이용할 수 없습니다.



변경금지. 귀하는 이 저작물을 개작, 변형 또는 가공할 수 없습니다.

- 귀하는, 이 저작물의 재이용이나 배포의 경우, 이 저작물에 적용된 이용허락조건을 명확하게 나타내어야 합니다.
- 저작권자로부터 별도의 허가를 받으면 이러한 조건들은 적용되지 않습니다.

저작권법에 따른 이용자의 권리는 위의 내용에 의하여 영향을 받지 않습니다.

이것은 [이용허락규약\(Legal Code\)](#)을 이해하기 쉽게 요약한 것입니다.

[Disclaimer](#)

Master's Thesis

Porosity tunable graphitic carbons
for energy applications

Myung Jun Kwak

School of Molecular Sciences
(Chemical Engineering)

Graduate School of UNIST

2016

Porosity tunable graphitic carbons
for energy applications

Myung Jun Kwak

School of Molecular Sciences

(Chemical Engineering)

Graduate School of UNIST


Porosity tunable graphitic carbons for energy applications

A thesis/dissertation
submitted to the Graduate School of UNIST
in partial fulfillment of the
requirements for the degree of
Master of Science

Myung Jun Kwak

1. 13. 2016

Approved by



Advisor

Ji-Hyun Jang

Porosity tunable graphitic carbons for energy applications

Myung Jun Kwak

This certifies that the thesis/dissertation of Myung Jun Kwak is
approved.

1. 13. 2016

signature



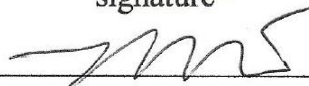
Advisor: Ji-Hyun Jang

signature



Hyun-Kon Song

signature



GunTae Kim

Abstract

With growing demand on energy sources, diminishing natural resources and increasing environment issues, the development of safe, no-pollution, low-cost and renewable energy systems where combustion no longer dominates has become a grand challenge nowadays. Among the various energy storage systems, supercapacitor and Zn-air batteries are considered as the most realizable and effective candidates due to their high efficiency, safety, durability, and low cost. Supercapacitor electrode requires the large surface area, good chemical stability, and high electrical conductivity because it stores charges by electrostatic adsorption/desorption of the electrolyte ions onto electrodes. Besides, in the case of the Zn-air battery, the development of highly efficient oxygen catalyst without precious metal including Pt, Ir, and Ru which facilitates the sluggish oxygen related reaction is required for real application.

This thesis covers the development of three-dimensional porous graphitic carbon structures and their applications to supercapacitor electrodes and oxygen electrocatalyst for Zn-air battery. The excellent property of porous carbon architectures for energy applications are mostly due to the large specific surface area with desirable porosity and the large amount of electrochemical active site density. This work suggests the promising way to fabricate highly efficient and durable carbon nanomaterials for energy-related applications.

Contents

Abstract	1
Contents	2
List of Figures	3
List of Tables	6
Chapter 1. Introduction of electrochemical energy storage devices	7
1.1 Overview	7
1.2. Supercapacitors	10
1.2.1 Brief overview	10
1.2.2 Working principles of Supercapacitor	12
1.3 Zinc Air battery	15
1.3.1 Introduction	15
1.3.2 Working principles of Zn air battery	17
1.4. References	19
Chapter 2. Synthesis and modification of Porous graphitic carbon foam with 3-Dimensional networks as high performance supercapacitor	20
2.1. Introduction	20
2.2 Experimental	21
2.2.1 Electrode fabrication and electrochemical measurement	21
2.3 Results and Discussion	23
2.4 Conclusions	35
2.5. Reference:	38
Chapter 3. Hierarchical porous nitrogen-doped graphitic carbon foam with 3-Dimensional networks as highly active oxygen catalyst for Zn-air battery	41
3.1. Introduction	41
3.2. Experimental Section	42
3.2.1. Synthesis	42
3.2.2. Characterization	42
3.2.3 Electrochemical Measurements	43
3.3. Results and Discussion	44
3.4. Conclusion.	69
3.4. References	70

List of Figures

Figure 1.1.1. The historical and projected energy demand trends. Adapted from.¹⁵ (Where 1 quad Btu is equal to 293 terawatt-hours (TWh))

Figure 1.1.2. A schematic integrated electrochemical energy system composed of fuel cells (FCs), solar hydrogen generators (SHs), electrolyzers (ELs), and redox flow batteries (FBs) to afford safe and clean environments

Figure 1.2.1 A typical Ragone plot indicating specific energy versus specific power for various energy storage systems.

Figure 1.2.2 Schematic diagrams of (a) a two-cell supercapacitor device made of nonporous electrode and (b) the electric double-layer structure on the basis of a positively charged electrode surface

Figure 1.2.3. Typical shaped carbon nanomaterials for supercapacitors.

Figure 1.3.1. Comparison of theoretical and practical energy densities of various batteries.

Figure 1.3.2 Schematic illustration of zinc-air battery.

Figure 2.1 (a) Raman spectra of 3dCF and 3dNCF with I_d / I_g ratio, (b) Nitrogen adsorption – desorption isotherm, (c-d) SEM image of 3dCF (c) and 3dNCF (d), (e-f) TEM images of 3dCF (e) and 3dNCF (f).

Figure 2.2 (a) XPS full spectra of 3dCF and 3dNCF. (b) High-resolution spectrum of the N 1s XPS peak of the 3dNCF. (c) Elemental composition of prepared samples.

Figure 2.3. TGA curves for different carbon precursors.

Figure. 2.4 (a) Cyclic voltammetry curves of 3DCF and 3dNCF at the scan rate of 10 mV s^{-1} in 6M KOH solution. (b) CV curves of 3D NCF electrode at a variety of scan rates from 5 to 100 mV s^{-1} . (c) Specific capacitance as a function of scan rate. (d) Galvanostatic charge/discharge plots of 3DCF and 3dNCF at a current density of 1 A g^{-1} . (e) GCD curves of 3dNCF electrode measured at various current densities from 1 to 15 A g^{-1} . (f) Specific capacitance change as a function of current density.

Figure. 2.5 (a) Nyquist plot of 3DNCF electrode in 6 M KOH electrolyte solution. (b) Cyclic stability of 3DNCF electrode as a function of cycle numbers. The inset shows the GCD curves at constant current of 4 A g⁻¹.

Figure. 2.6 (a) Cyclic voltammetry curves of 3DNCF-based symmetric supercapacitor at different scan rates. (b) Specific capacitance versus scan rates. (c) Galvanostatic charge/discharge curves of symmetric supercapacitor at different current densities. (d) Specific capacitance of symmetric supercapacitor based on total mass of active materials in two electrodes versus current density.

Figure. 2.7 (a) Cycling performance of 3D NNCF symmetric supercapacitor at constant current density of 2 A g⁻¹ for 10000 cycles. The inset shows the GCD curves. (b) Nyquist plots of symmetric supercapacitor before and after stability test. (c) Energy density versus power density of 3DNCF symmetric supercapacitor.

Figure. 3.1. TGA curves of PVP, FeCl₃, and PVP/FeCl₃

Figure 3.2. (a) SEM image of the 3dNCF. (b, c) TEM image of the 3dNCF-800. (d) TEM image of 3dNCF-800 with corresponding elemental mapping. (e) Raman spectra of 3dNC and 3dNCFs. (f) Nitrogen adsorption/desorption of the 3dNC and 3dNCFs. (g)BJH curves of 3dNC and 3dNCFs.

Figure 3.3 SEM and TEM images of 3dNC-800 with different magnifications

Figure 3.4. Additional TEM images of 3dNCF-800 with different magnifications

Figure 3.5. TEM images of resulting 3dNCF-900

Figure 3.6. TEM image of resulting 3dNCF-1000

Figure 3.7. XPS survey spectra of prepared 3dNC and 3dNCF-Xs

Figure 3.8. High-resolution N1s XPS signals for 3dNC-800 (a), 3dNCF-800 (b), 3dNCF-9000 (c), and 3dNCF-1000 (d). The signals deconvoluted into four energy components around 398.0, 398.9, 400.7, and 402.7 eV, indicating the presence of pyridinic-, pyrrolic-, graphitic- and oxidized-N, respectively.

Figure. 3.9 (a) Atomic content of 3dNC and 3dNCF-X. (b) Atomic contents of pyridinic N, pyrrolic N, graphitic N, and oxidized N calculated in N1s XPS spectra.

Figure. 3.10. Cyclic voltammetry curves of the prepared catalysts and commercial Pt/C catalyst in 0.1 M KOH saturated with N₂ (Black curves) or O₂ (Red curves)

Figure 3.11. a) Linear sweep voltammetry (LSV) of 3dNC, 3dCF, and 3dNCF-X in oxygen-saturated 0.1 M KOH with a RDE rotation rate of 1600 rpm. b) LSV curves of 3dNCF-800 in oxygen-saturated 0.1 M KOH at various rotating speeds. c) H₂O₂ yields plots of 3dNC, 3dNCF-X, and Pt/C catalyst. d) Tafel plots measured in Oxygen-saturated 0.1M KOH. e) LSV curves for 3dNCF-X and Pt/C in 0.5 M H₂SO₄ for metal-free catalysts and 0.1 M HClO₄ for Pt/C. For all the RDE and the RRDE tests, the mass loading of catalysts was 20 ug_{pt} cm⁻² for Pt/C and 0.6 mg cm⁻² for carbon catalysts. f) LSV curves of 3dNCF-800, RuO₂ and commercial Pt/C catalyst on an RDE in 0.1 M KOH with a RDE rotation speed 1600 rpm. All of the LSV scan rate is fixed at 10 mVs⁻¹

Figure 3.12. Electrochemical impedance spectroscopy (EIS) analysis of the catalysts. EIS were measured in O₂-saturated 0.1 M KOH at -0.115 V vs. Ag/AgCl with 5 mV ac potential from 10 kHz to 0.01 Hz. The catalyst loading was 0.6 mg/cm² for all catalysts

Figure. 3.13. LSV curves of 3dNC-800 (a), 3dNCF-900 (b), 3dNCF-1000 (c), Pt/C (d) in oxygen-saturated 0.1 M KOH with various rotating speeds.

Figure. 3.14. Current-time (i-t) Chronoamperometric response (a) for 3dNCF-900 and Pt/C kept at -0.25 V versus Ag/AgCl in N₂- and O₂-saturated 0.1 M KOH electrolyte. The arrow indicates the O₂ injection. (b) The arrow indicates the addition of 3 M Methanol.

Figure. 3. 15. LSV curves of 3dNCF-800 (a), 3dNCF-900 (b), 3dNCF-1000 (c), Pt/C (d) in oxygen-saturated 0.5 M H₂SO₄ for metal-free catalysts and 0.1 M HClO₄ for Pt/C with various rotating speeds

Figure 3. 16 Linear sweep voltammograms (LSV) of 3dNCF-800 on a rotating disk electrode at 1600 rpm in O₂ saturated 0.1 M KOH with and without NaSCN.

Figure 3.17. Two electrode Zn-air battery performance. Discharge curves of the Zn-air batteries using 3dNCF-800, 3dNCF-900 and Pt/C catalyst at 25 mA cm⁻² (a). Discharge/charge cycling test at a current density of 25 mA cm⁻² using the 3dNCF-900 and Pt/C as air electrodes.

List of Tables

Table 2.1 Summarized chemical composition for 3dCF and 3dNCF.

Table. 2.2 Comparison of the electrochemical performance of the as-prepared 3dNCF with previously reported N-doped carbon materials.

Table 3.1. Specific surface areas (SSA) and total pore volume and average pore diameter distribution of 3DNCs.

Table 3.2. Atomic content and nitrogen composition of 3dNC and 3dNCF-X calculated from the XPS survey spectra.

Table 3.3. Comparison of ORR performance in 0.1 M KOH electrolyte of 3dNCF and with literature values.

Chapter 1. Introduction of electrochemical energy storage devices

1.1 Overview

With growing demand on energy sources, diminishing natural resources, increasing environment issues, the development of safe, no-pollution, low-cost and renewable energy systems where combustion no longer dominates has become a grand challenge nowadays¹ (Figure 1.1). Although renewable and sustainable electricity generation sources such as solar, wind, and wave could be candidates for conventional energy fuels, it is still important to find desirable electrical energy conversion and storage systems possessing high efficiency to save extra energy hence to meet the increased energy demands² (Figure 1.2). Consequently, the search for the next generation of energy-storage materials and devices such as supercapacitors and rechargeable batteries with pollution free operation, high efficiency, and a long cycling life is extremely important³. In this thesis, we focused on the fabrication of the three-dimensional graphitic carbon foam with high specific surface areas and desirable surface functionality, which are favorable characteristics for supercapacitor electrode and air electrode catalysts for Zn-air battery. The remarkable performance of each device is attributed to the enhanced mass and ion transport through porous architectures as well as the increased electrical conductivity and active site densities by heteroatom doping.

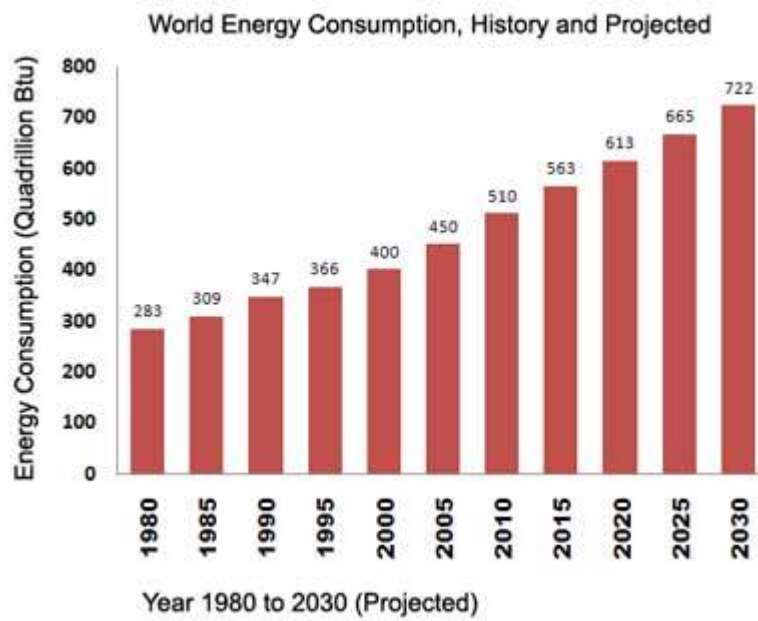


Figure 1.1.1 The historical and projected energy demand trends. Adapted from.¹⁵ (Where 1 quad Btu is equal to 293 terawatt-hours (TWh))

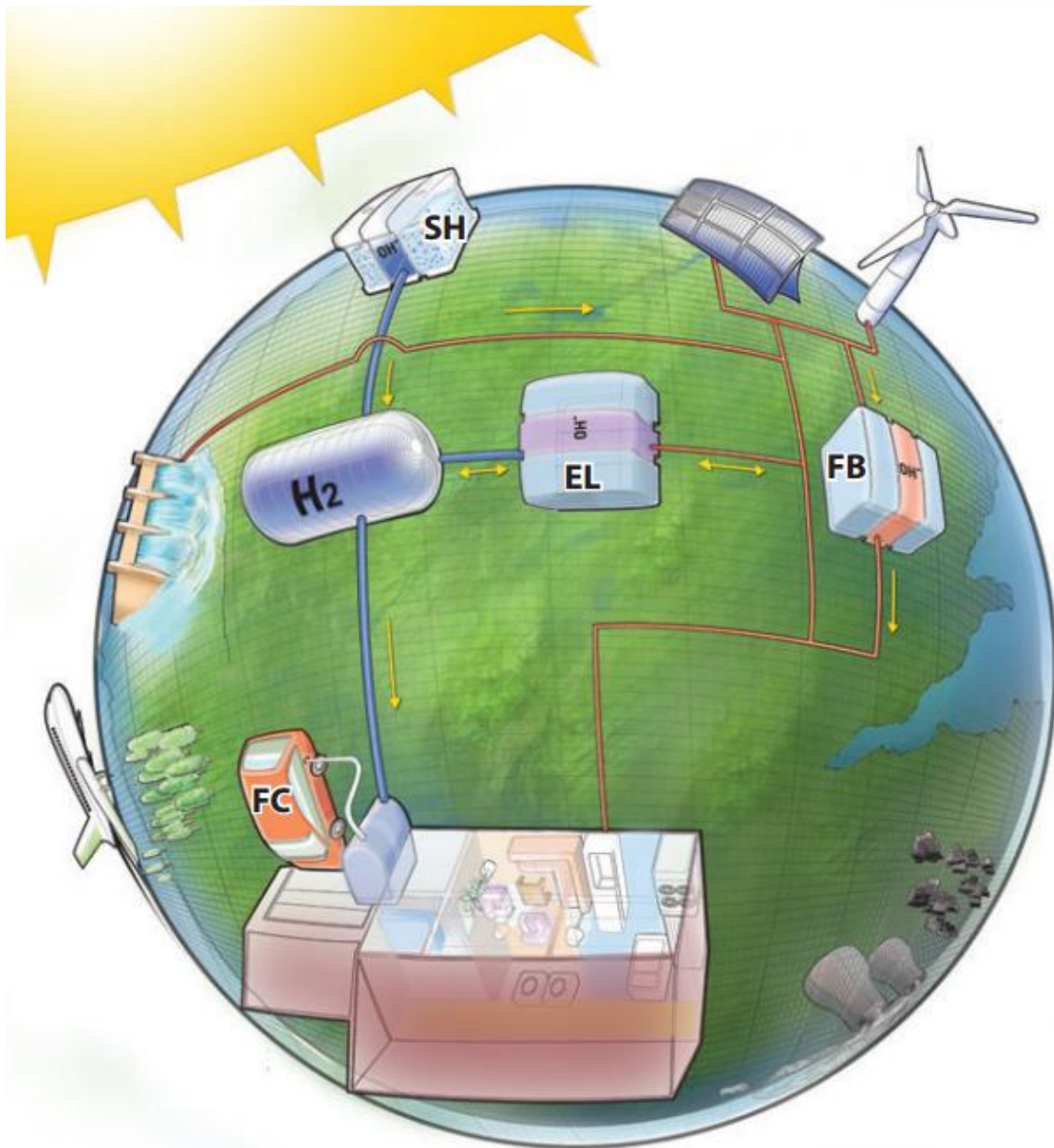


Figure 1.1.2 A schematic integrated electrochemical energy system composed of fuel cells (FCs), solar hydrogen generators (SHs), electrolyzers (ELs), and redox flow batteries (FBs) to afford safe and clean environments. Adapted from ¹

1.2. Supercapacitors

1.2.1 Brief overview

The typical relationship between the power and energy density of stored electrical energy on several energy storage devices is easily compared by using so-called Ragone plot depicted in Figure 1.1. The areas corresponding to each device could be a simple guideline for their specific energy and power outputs^{4,5}. It is seen that supercapacitors occupy a region between conventional capacitors and batteries. Among the energy storage devices supercapacitor is a rising energy storage system because it can exhibit higher power and energy density than batteries and traditional dielectric capacitors³, respectively. Supercapacitor is an promising power solution to numerous applications including transportation, renewable energy power generations due to high efficiency, long cycling lifetime, and capable use of wide temperature range, etc^{6,7}.

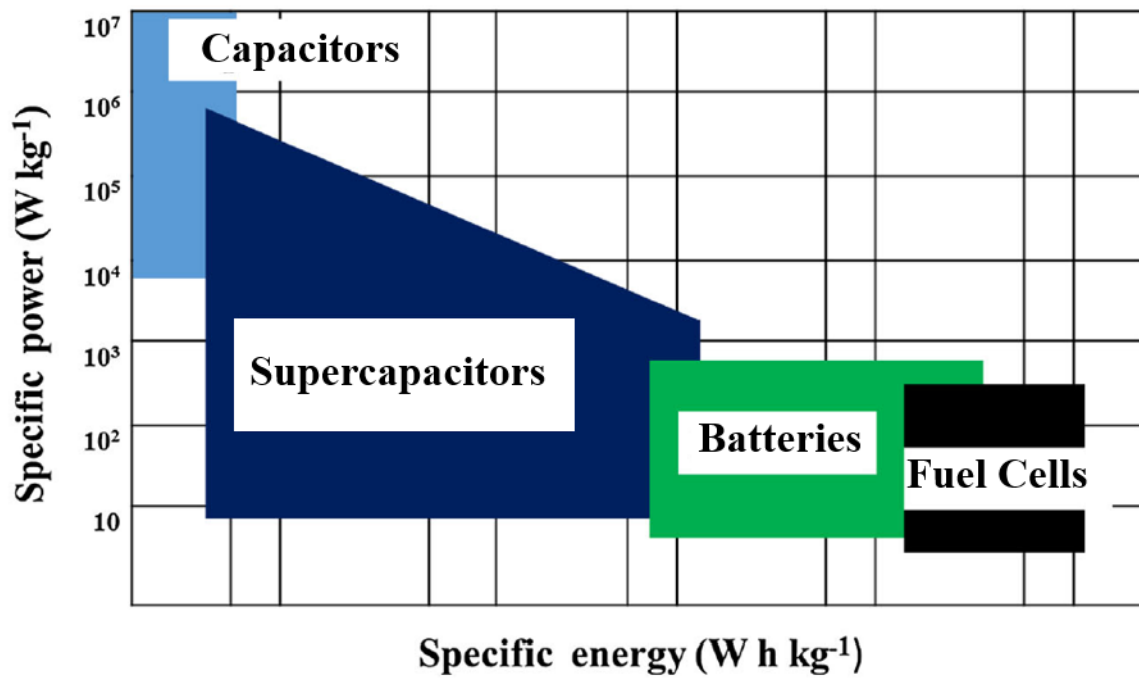


Figure 1.2.1 A typical Ragone plot indicating specific energy versus specific power for various energy storage systems. Adapted from [3-4]

1.2.2 Working principles of Supercapacitor

In briefly, electric double-layer capacitor (EDLC) composed of two electrodes separated by selective transmitting membranes in electrolyte stores charges by non-faradaic process without charge transfer process across at the surface of electrode, which is similar to the basic principles of conventional capacitors⁷. One of the challenges is an inverse relationship between energy and power in the supercapacitor, i.e. a higher power with fast energy releasing rate induces the decreased energy capacity and vice versa. So lots of attention have been paid to supercapacitors to desirable performance with both high power density and energy density needed by applying new technology such as nanotechnology. One of the potential electrode materials for supercapacitors is allotropes carbon nanomaterials (Figure 1.2.3.) which usually possesses high surface area, high electrical conductivity as well as desirable porous channels.

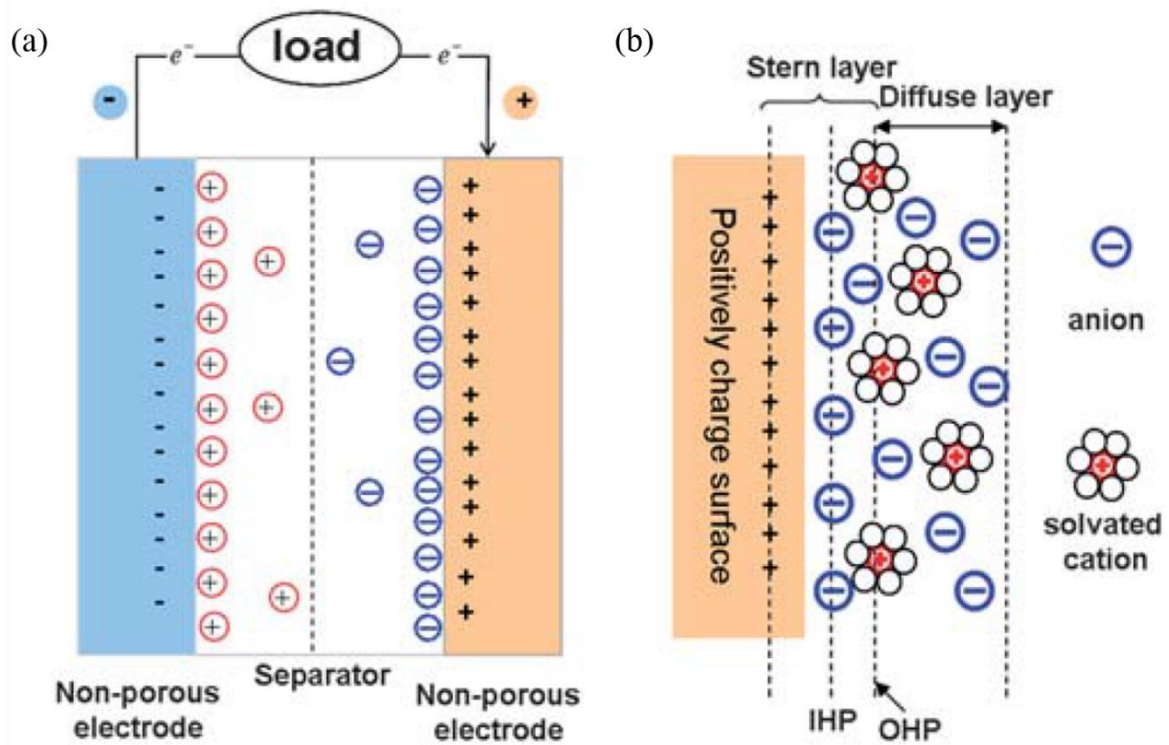


Figure 1.2.2 Schematic diagrams of (a) a two electrode supercapacitor device made of nonporous electrode and (b) the electric double-layer on the basis of a positively charged electrode surface. Adapt from⁸

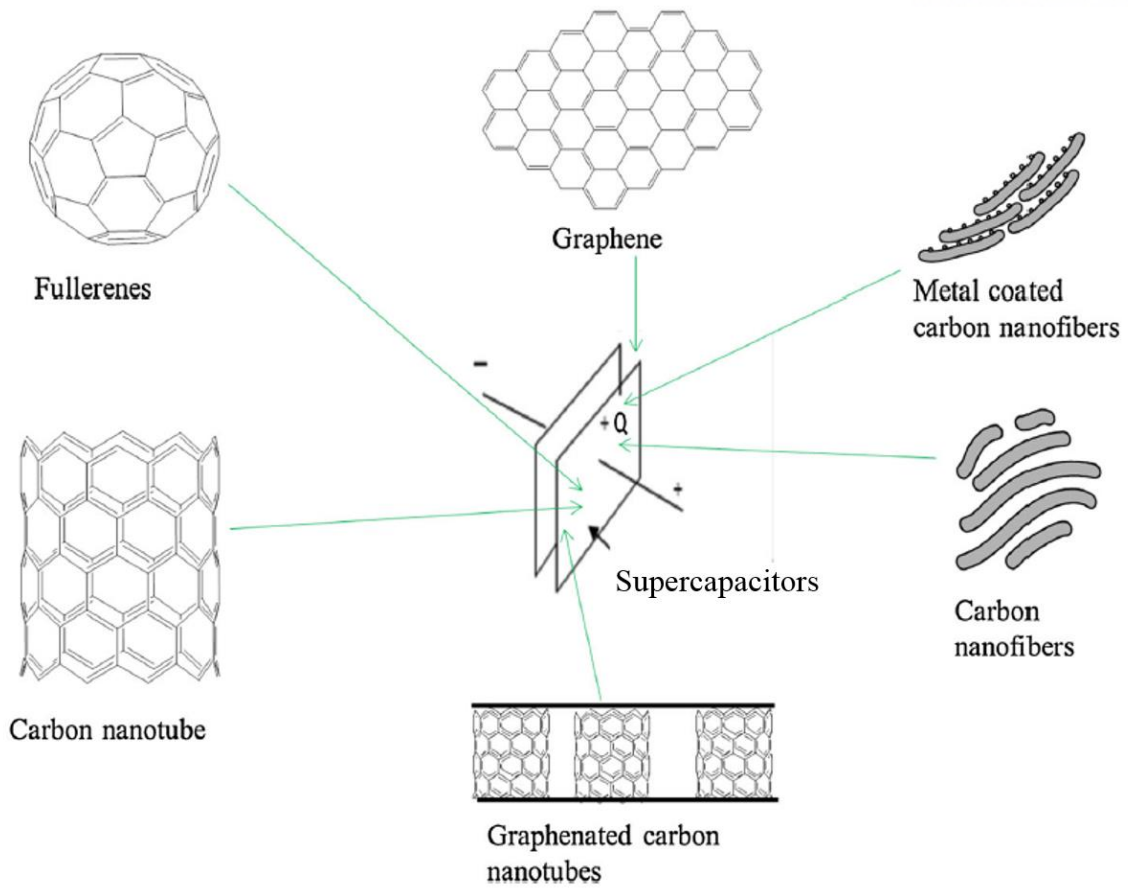


Figure 1.2.3. Typical shaped carbon nanomaterials for supercapacitors³.

1.3 Zinc Air battery

1.3.1 Introduction

Metal-air batteries are another candidate for future generation because they possess higher energy density in comparison with that of other energy storage devices⁹ (Figure 1.3.1) with light-weighted structures by employing the oxygen from the air as one of the reaction reactant². Although lithium-air batteries possess lots of potentials in terms of its high practical and theoretical energy density among all the various energy storage systems, the high reactivity of lithium with air and humidity bring about a high safety risk. In this regard, the zinc-air battery is the most promising one due to its safe, earth abundant, low-cost, environmental friendly features, which make it attractive electrical energy storage and delivery systems for portable devices as well as electric vehicles^{10, 11}.

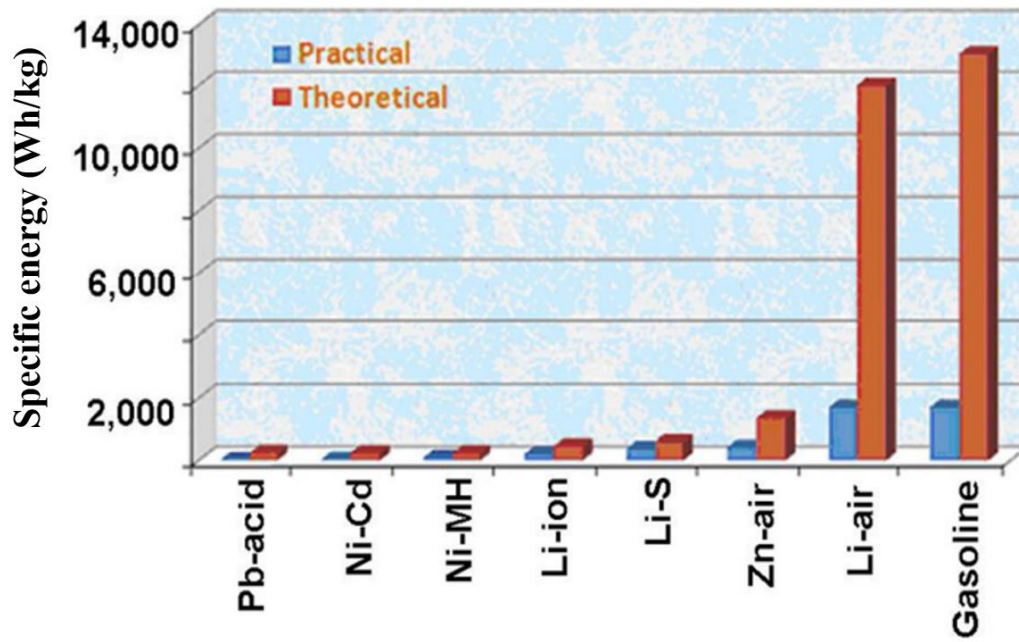
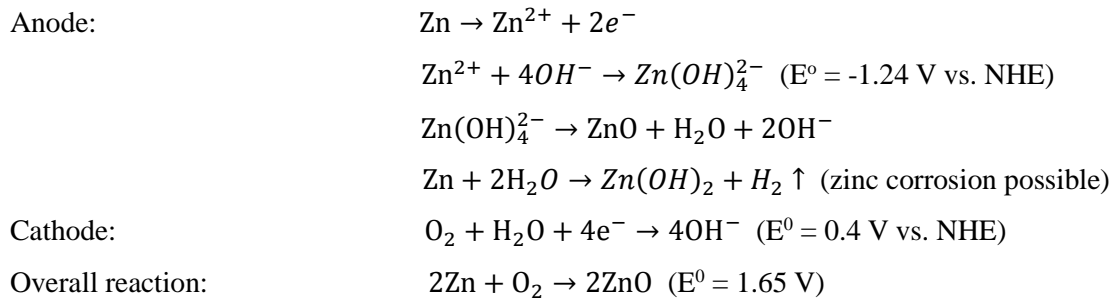


Figure 1.3.1. Comparison of theoretical and practical energy densities of various batteries (adapted from).⁹

1.3.2 Working principles of Zn air battery

Zinc-air cell is composed of a zinc electrode (anode), an alkaline electrolyte (KOH) and an air electrode (cathode) as briefly depicted in figure 1.3.2.¹¹ Zinc-air batteries generate electricity through a redox reaction between metal and oxygen in air; Zinc-air batteries breath air. Specifically, during discharging process, diffused air from the air is reduced to hydroxide ions through the oxygen catalysts (cathode) with the electrons generated from the electrochemical oxidation of the zinc electrode (anode). The involved chemical reactions during discharging process are described as follows.¹⁴



On the charging process, the reverse process occurs including oxygen evolution at the air electrode and zinc deposition at the zinc electrode.

Since the oxygen reaction is sluggish, it is highly desirable to develop a suitable catalyst that can accelerate the oxygen reduction and oxygen evolution reaction (ORR/OER)¹². To date, the most efficient catalysts to facilitate both the ORR and the OER are based on the noble metal catalysts (Pt, Rb, Ir, etc). However, their scarcity and the high cost limit the wide application of these catalysts. Therefore, it is in demand to develop the alternatives with efficient, low-cost and durable features for oxygen electrode in order to commercialize the zinc-air battery system.¹³

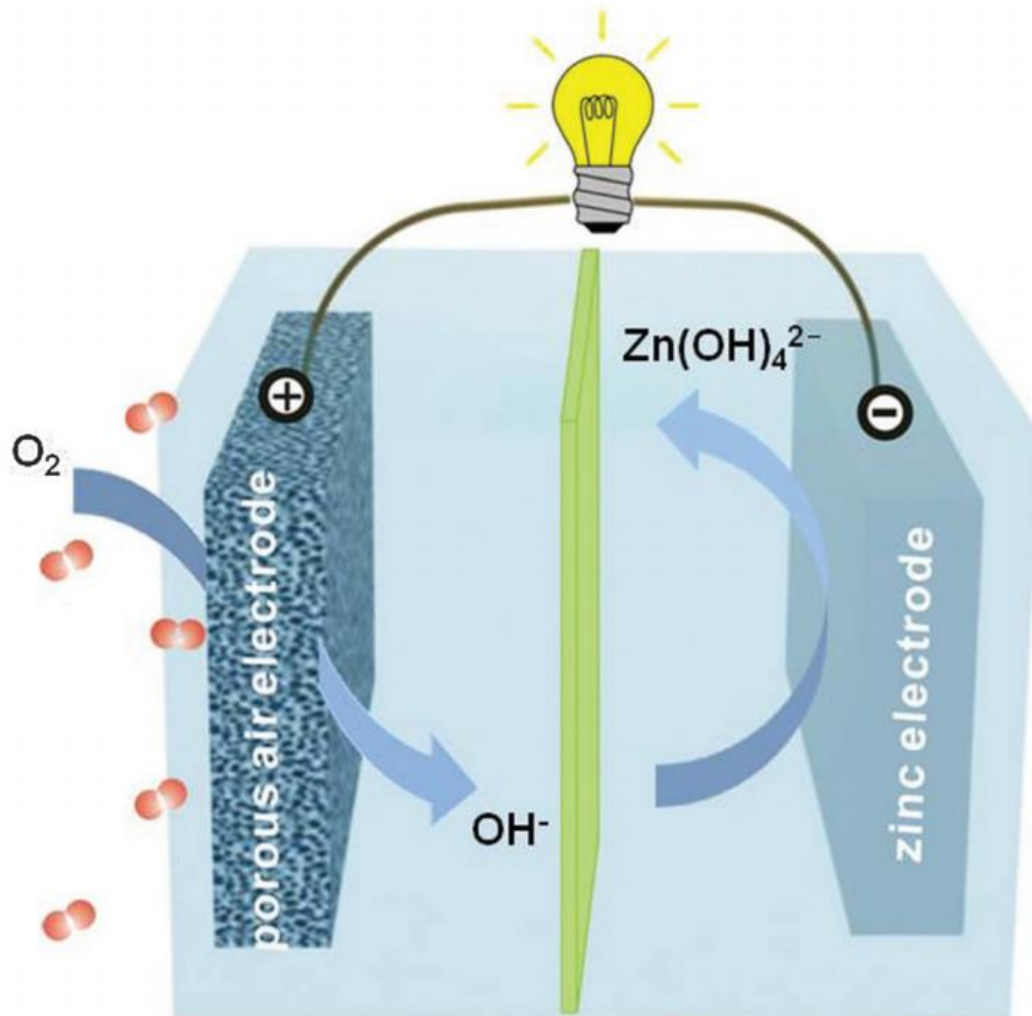


Figure 1.3.2 Schematic illustration of zinc-air battery. (Adapted from)¹¹

1.4. References

1. Gu, S.; Xu, B.; Yan, Y., Electrochemical energy engineering: a new frontier of chemical engineering innovation. *Annual review of chemical and biomolecular engineering* **2014**, *5*, 429-454.
2. Caramia, V.; Bozzini, B., Materials science aspects of zinc–air batteries: a review. *Materials for Renewable and Sustainable Energy* **2014**, *3* (2), 1-12.
3. Mombeshora, E. T.; Nyamori, V. O., A review on the use of carbon nanostructured materials in electrochemical capacitors. *International Journal of Energy Research* **2015**, *39* (15), 1955-1980.
4. Kötz, R.; Carlen, M., Principles and applications of electrochemical capacitors. *Electrochimica Acta* **2000**, *45* (15), 2483-2498.
5. Jian, L.; Xiaoqian, C.; Alexey, S.; Michael, K., Review of electrochemical capacitors based on carbon nanotubes and graphene. *Graphene* **2012**, *2012*.
6. Schainker, R. B. In *Executive overview: energy storage options for a sustainable energy future*, Power Engineering Society General Meeting, 2004. IEEE, IEEE: 2004; pp 2309-2314.
7. Halper, M. S.; Ellenbogen, J. C., Supercapacitors: A brief overview. *The MITRE Corporation, McLean, Virginia, USA* **2006**, 1-34.
8. Zhang, L. L.; Zhou, R.; Zhao, X., Graphene-based materials as supercapacitor electrodes. *Journal of Materials Chemistry* **2010**, *20* (29), 5983-5992.
9. Wang, J.; Li, Y.; Sun, X., Challenges and opportunities of nanostructured materials for aprotic rechargeable lithium–air batteries. *Nano Energy* **2013**, *2* (4), 443-467.
10. Neburchilov, V.; Wang, H.; Martin, J. J.; Qu, W., A review on air cathodes for zinc–air fuel cells. *Journal of Power Sources* **2010**, *195* (5), 1271-1291.
11. Li, Y.; Dai, H., Recent advances in zinc-air batteries. *Chemical Society Reviews* **2014**, *43* (15), 5257-5275.
12. Liang, Y.; Li, Y.; Wang, H.; Zhou, J.; Wang, J.; Regier, T.; Dai, H., Co₃O₄ nanocrystals on graphene as a synergistic catalyst for oxygen reduction reaction. *Nature materials* **2011**, *10* (10), 780-786.
13. Zhang, J.; Xia, Z.; Dai, L., Carbon-based electrocatalysts for advanced energy conversion and storage. *Science advances* **2015**, *1* (7), e1500564.
14. D. Linden and T. B. Reddy, *Handbooks of Batteries*, McGraw-Hill, 2001
15. U.S. Energy Information Administration, International Energy Annual 2003, System for the analysis of Global Energy Markets(2006)

Chapter 2. Synthesis and modification of Porous graphitic carbon foam with 3-Dimensional networks as high performance supercapacitor

2.1. Introduction

Electrochemical capacitors or supercapacitors have been attracted to be the most desirable candidate to meet the increasing demand on electricity storage due to their long term cycle stability, fast charging-discharging rate, and high power density¹. The electrical energy is charged by electrostatic adsorption/desorption of the electrolyte ions onto a supercapacitor electrode, which induces an electrochemical double layer capacitance (EDLC) that is mostly affected by the surface area and electrical conductivity of the electrode. To meet the required characteristics for supercapacitor, porous carbon nanomaterials are recognized as the promising electrode material owing to its low cost, large surface area (SSA), excellent chemical stability, good electrical conductivity, and long cycling life. Metal oxide materials including Ni(OH)₂ and Co(OH)₂ or conducting polymers based materials such as polyaniline have been introduced to overcome the limitation associated with the porous carbon materials. These kind of materials store electric charges by fast redox reactions at the surfaces, which is widely known as pseudocapacitance. Although the pseudocapacitance possesses enhanced capacitances than EDLCs, they exhibit rather slower charge and discharge rates than EDLCs due to their faradaic reactions in their charge/discharge process. Moreover, the low conductivity of metal oxide induces large dead volumes and decreases the specific capacitance. Another facile and effective strategy to modify the properties of carbon nanomaterials and improve the capacitance is introducing heteroatoms such as B, N, P, and S into carbon structures. Incorporation of the heteroatoms affects the carbon materials' pseudocapacitance and surface adsorption properties as well^{1, 2}. In particular, nitrogen doping has been thought of one of the efficient ways to improve the EDLCs due to the synergistic effects induced by the nitrogen incorporation which induces the better conductivity and surface wettability along with adsorption properties results in facilitated electrochemical reaction on the carbon surface.³

Our groups previously reported the fabrication strategy to prepare the three-dimensional graphene nano-networks (3dGN) via precursor assisted-CVD by employing the silica as a sacrificial template, iron salts (FeCl₃) as graphitization agents, and polyvinylalcohol (PVA) as a carbon precursor⁴. The resultant 3dGN with high surface area up to ~1025 m²g⁻¹ shows high conductivity of ~52 S/cm hence exhibit high specific capacitance of 245 F/g in a H₂SO₄ solution. One of the major advantages of this preparation method is the easy modification of the surface and chemical property of the fabricated graphitic carbon networks by controlling the starting precursors.

Here, we report the hierarchical porous carbon foam by employing various carbon precursors including starch and poly vinyl pyrrolidone (PVP). Starch, a kind of biomass, has become a well-known pore-forming agent for the preparation of ceramics during pyrolysis process.³⁰ It has been reported that

the type and amount of starch determines the pore morphology and the pore volume, respectively.³⁰ PVP is also famous chain polymers used as a encapsulation agent especially for metals surfaces to avoid oxidation. The nitrogen embedded in the pyrrolidone was expected to be nitrogen sources incorporated to the carbon structures during pyrolysis. The resultant starch derived three-dimensional porous carbon foam (3dCF) exhibits the high surface area of 1540 m²g⁻¹ with specific capacitance of 152 F g⁻¹ at 1 A g⁻¹. The successful nitrogen incorporation into carbon nanostructure is obtained by employing PVP as a carbon source including nitrogen. The PVP derived three-dimensional nitrogen doped carbon foam (3dNCF) shows the specific capacitance of 270 F g⁻¹ at 1 A g⁻¹ due to the high specific surface area (~1148 m²g⁻¹) with abundant active site dispersion over hierarchical pores to facilitate rapid charge transfer, high charge capacity, easy electrolyte access, and adequate mass transport, which can be a suitable electrode materials for EDLCs.

2.2 Experimental

2.2.1 Electrode fabrication and electrochemical measurement

The working electrode was prepared by mixing a weight ratio of 8:1:1 of electroactive material (3DCF and 3dNCF), acetylene black and polyvinylidene fluoride (PVDF) in N-methyl pyrrolidone (NMP) solvent to form a well-dispersed slurry. Then, the prepared mixture was pressed (coated) on to a nickel form used for current collector and dried at 90 °C in a convection oven for 24 hours to evaporate the solvent. The electrochemical properties of the prepared electrodes were evaluated by employing a conventional three electrode cell in 6 M KOH electrolyte. A mercury – mercury oxide (Hg/HgO) electrode and platinum wire were used as the reference and counter electrodes, respectively. Two electrode symmetric cell system was applied to further investigate the device performance of 3dNCF electrode. The symmetric supercapacitor was assembled by using a two 3DNCF on nickel plate as positive and negative electrode, a filter paper as the separator and 6 M KOH aqueous solution as the electrolyte. The cyclic voltammetry (CV) and galvanostatic charge/discharge operation were conducted on a VMP3 biologic potentiostat. The electrochemical impedance spectroscopy (EIS) measurement was investigated in the frequency range of 100 mHz to 100 kHz by using VersaSTAT3 (Princeton Applied Research). The specific capacitance (F g⁻¹) was determined from the CV and GCD curves according to the following equations⁵:

$$C = \frac{\int idV}{2v\Delta V} \dots\dots\dots (1)$$

$$C = \frac{I\Delta t}{\Delta V} \dots\dots\dots (2)$$

For single electrode capacitance:

$$C_s = 4 \times C \dots\dots\dots (3)$$

where $\int idV$ is the integral area under the CV curve, v is the scan rate, Δt is the discharge time, I is the discharge current, ΔV is the potential window, and m is the mass of the electroactive material on the two electrodes. Additionally, the energy density (W h kg^{-1}) and power density (W kg^{-1}) of the symmetric cell were determined from the discharge curves by using the following equations.

$$E = \frac{C (\Delta V)^2}{7.2} \dots\dots\dots (4)$$

$$P = \frac{E \times 3600}{\Delta t} \dots\dots\dots (5)$$

where C means the specific capacitance of the symmetric cell, P refers to the power density, E stands for the energy density, Δt denotes the discharge time and ΔV is the voltage drop during discharge.

2.3 Results and Discussion

The overall preparation process is similar to the fabrication method already reported in our group.⁴ Briefly, the prepared self-assembled SiO₂ templates was coated by the carbon precursors solutions mixed with optimized amount of FeCl₃. The metal salts FeCl₃ was reported by effective activation-graphitization agents that can produce a porous structure with sufficient micro- and mesopores for a high surface area.⁶ After drying, the prepared powder was pyrolyzed at 900°C under H₂/Ar flow atmosphere followed by leaching process. The prepared samples are denoted to three-dimensional carbon foam (3dCF) and three-dimensional nitrogen doped carbon foam (3dNCF) for starch derived and PVP derived, respectively.

Raman spectra of 3dCF and 3dNCF demonstrates the graphitic nature of each samples with a G-peak located at 1581 cm⁻¹ and a D-peak at 1341 cm⁻¹ associated with the stretching of sp²-bonded pairs and the sp³ defect sites, respectively⁷ (Fig. 2 a). Although the position of D and G peaks remain unchanged, the intensity ratio of I_D/I_G increased from 3dNCF to 3dCF probably due to the different chemical composition and porous structures of each sample.

The porous architecture of the samples was investigated by nitrogen adsorption-desorption isotherms (Fig. 2 b), which shows a type-IV plot with a rapid increase at a relatively high pressure ($P/P_0 = 0.80 - 0.99$) indicating that the pore volume is mostly attributed to mesopores.⁸ The Barrett-Emmett-Teller (BET) surface area of the 3dCF is 1564 m² g⁻¹, larger than that of 3dNCF (1064 m² g⁻¹). The increased surface area of starch derived carbon is probably due to the generation of pores from generation of lots of volatile gases during thermal pyrolysis process (Figure 2.3).⁹ The average diameter of mesopores from the Barrett-Joyner-Halenda (BJH) equation is 9.22 nm and 7.33 nm for 3dCF and 3dNCF, respectively, which implies that the resulting porosity can be tunable by employing the various carbon precursors even though the same fabrication process is attempted. Besides the porosity influenced by the precursor, the mesopores were also generated when the precursor is decomposed and segregated on the surface of the iron frames upon cooling and the aggregated iron particles are leached from the carbon structures.⁴

A scanning electron microscopy (SEM) and transmission electron microscopy (TEM) of 3dCF (Fig. 2c, e) and 3dNCF carbon (Fig. 2 d, f) reveal the interconnected hierarchical porous structures with mesopores. The nanoporous structures with high surface area with sufficient active site dispersion over hierarchical pores can enhance the mass transport by reducing the diffusive resistance as well as provide easy ion transport by shortening the diffusion pathways^{10,11}, which are important in developing excellent capacitance electrodes.

Overall, the morphological characteristics confirm that the hierarchical porous graphitic carbon architectures is successfully fabricated by various carbon precursors with large surface area accompanied by micro- and meso- pores, which are appropriated for both high-rate performance and

high-density energy storage.¹²

X-ray photoelectron spectroscopy measurements were performed to analyze the elemental composition of the carbon nanostructures (Fig. 3). As expected, XPS survey scans show that the starch derived carbon contains C (86.7 at %) and O (13.3 at %) and the PVP derived carbon is composed of C (90.47 at %), O (5.38 at %), and N (4.08 at %) (Fig. 3a, c), which demonstrate the successful incorporation of nitrogen atoms to the carbon structure by employing the PVP as carbon precursor. The XPS scan also confirm the sacrificial SiO₂ template and reduced iron catalyst completely leached away. The high-resolution N1s peak for PVP derived carbon is decomposed into 4 peaks located at 398 eV, 399 eV, 400.7 eV, and 402.6 eV which can be assigned to pyridinic-N (17.75 at%), pyrrolic-N (4.19 at%), graphitic-N (66.07 at %), and oxidized-N (11.98 at%), respectively, on the basis of their binding energies.¹³ The pyrrolic and pyridinic nitrogen species in the carbon nanostructures could induce the pseudocapacitance enhancement whereas the graphitic nitrogen configuration enhances the electronic conductivity of carbon materials, which is highly needed for electrodes with high conductivity.¹⁴ We believe that the tuned nitrogen content which increases the wettability to the electrolyte and the higher surface area in PVP derived carbon have favorable multiple synergistic effects to enhance the electrochemical reactivity and electronic conductivity, which prompts to the exceptional performance as well.

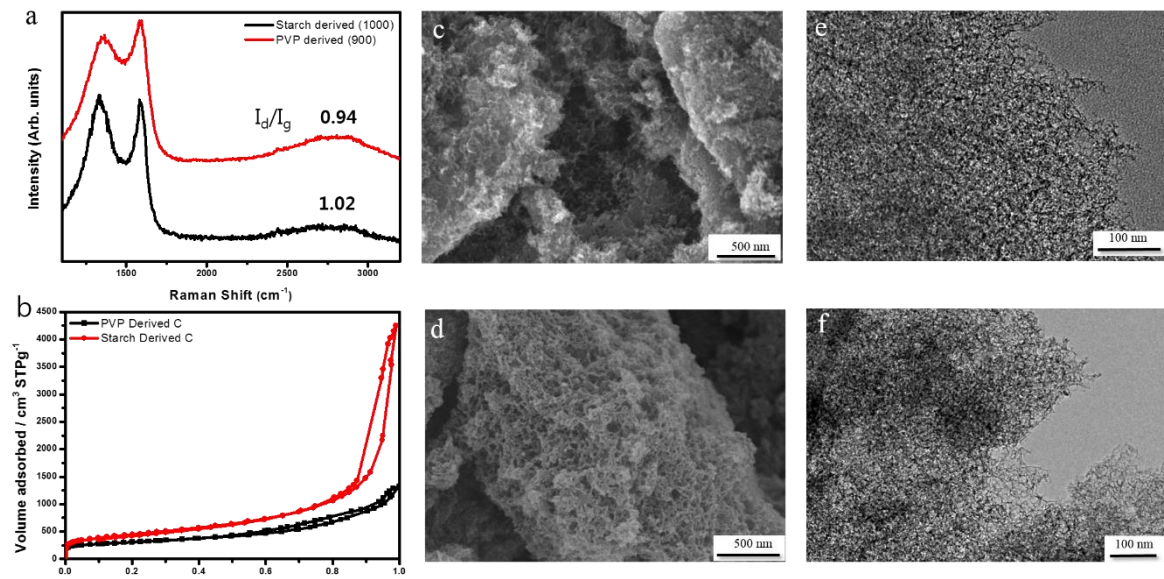


Figure 2.1 (a) Raman spectra of 3dCF and 3dNCF with I_d / I_g ratio, (b) Nitrogen adsorption – desorption isotherm, (c-d) SEM image of 3dCF (c) and 3dNCF (d), (e-f) TEM images of 3dCF (e) and 3dNCF (f).

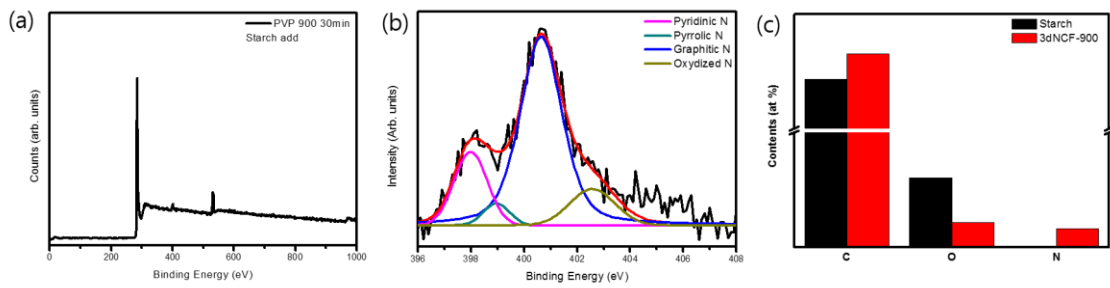


Figure 2.2 (a) XPS full spectra of 3dCF and 3dNCF. (b) high-resolution spectrum of the N 1s XPS peak of the 3dNCF. (c) elemental composition of prepared samples.

Sample	C at%	O at%	N at%	S_{BET} ($\text{m}^2 \text{g}^{-1}$)
Starch (rough)	86.7	13.3	0	1564
3dNCF-900	90.47	5.38	4.08	1064

Table 2.1 Summarized chemical composition for 3dCF and 3dNCF.

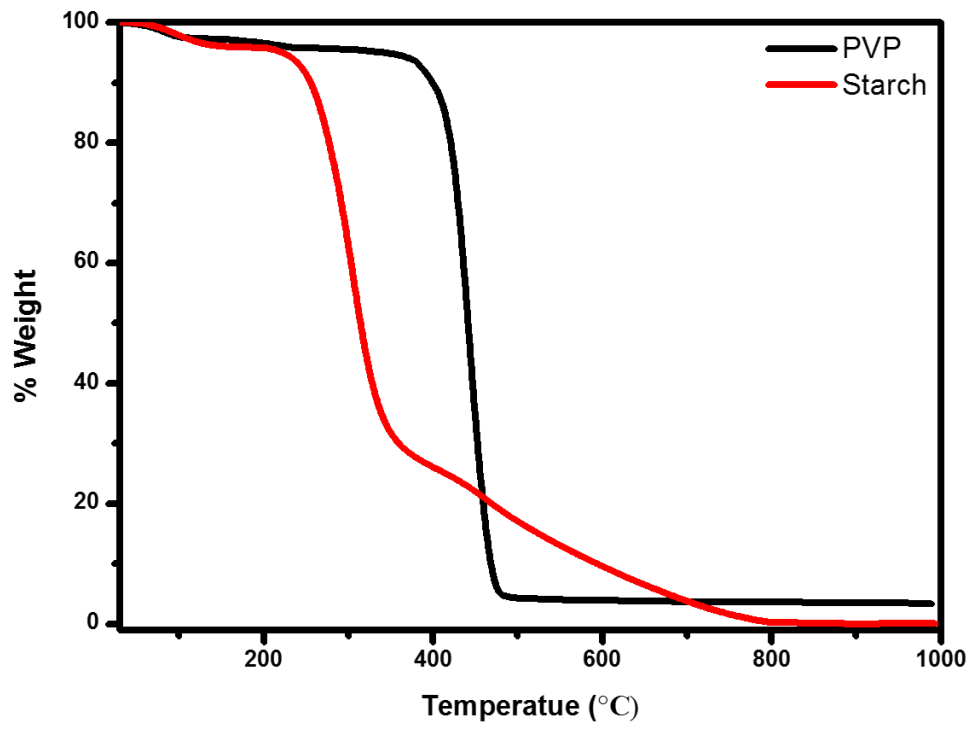


Figure 2.3. TGA curves for different carbon precursors.

The electrochemical performance of the 3dCF and 3dNCF electrode were measured by using cyclic voltammetry (CV), galvanostatic charge–discharge and electrochemical impedance spectroscopy (EIS) measurements in three electrode system in an aqueous 6 M KOH electrolyte solution and the results are displayed in Figure 2.4. The CV curves of the 3dCF and 3dNCF electrodes at a scan rate of 10 mV s⁻¹ are shown in Figure 2.4 a. Both curves clearly exhibits the typical rectangular shape illustrating the ideal capacitive behavior of each electrode. Comparatively, the 3dNCF electrode showed larger integrated area than that of 3dCF as expected, which demonstrates a superior electrochemical property of 3DNCF. In addition, Figure 2.4b shows the CV curves of the 3DNCF electrode at a variety of scan rates in the potential range of -1 to 0 V. The shape of the CV curves clearly exhibit the electrochemical double layer characteristics. The deviation from the rectangular shape of CV curves with increasing scan rates (at higher scan rates) indicates the deterioration of the electrochemical performance. This phenomenon may be due to the mass transport limitation of K⁺ ions from the electrolyte to the inner part of the electroactive materials.¹⁵⁻¹⁷ As the scan rate increases, the ions present in the electrolyte solution will transfer rapidly from the bulk electrolyte solution to the electrode/electrolyte interface, but relatively slow diffusion rate of ions from electrode/electrolyte interface to the inner electrode materials doesn't satisfy the electrochemical adsorption and desorption of electrode materials (parts of the electrode materials are inaccessible). Hence, most of the ions are accumulated near the electrode/electrolyte interface and resulting to the polarization of the electrode materials.

From CV graphs, the specific capacitance of 3dCF and 3dNCF electrode can be determined from equation (1). The specific capacitance of the materials as a function of scan rate is displayed in Figure 2.4c. At the same scan rate of 5 mV s⁻¹, a specific capacitance value of 182 and 265 F g⁻¹ is measured for 3dCF and 3dNCF, respectively. The 3DNCF possesses a higher capacitance value compared to 3dCF, which highlights the positive effect of nitrogen doping in turn enhance the electrochemical activity of carbon materials (wettability and charge transport). Moreover, the 3DNCF exhibited the specific capacitance values of 240, 221, 199, 182, 168 and 153 F g⁻¹ at the scan rates of 10, 20, 40, 60, 80 and 100 mV s⁻¹, respectively. Although, the specific capacitance drops gradually due to more serious polarization with rising the scan rate, 54% of the initial capacitance can be still preserved as the scan rate increases from 5 to 100 mV s⁻¹. This result clearly suggests the better rate capability of the as-prepared 3dNCF electrode.

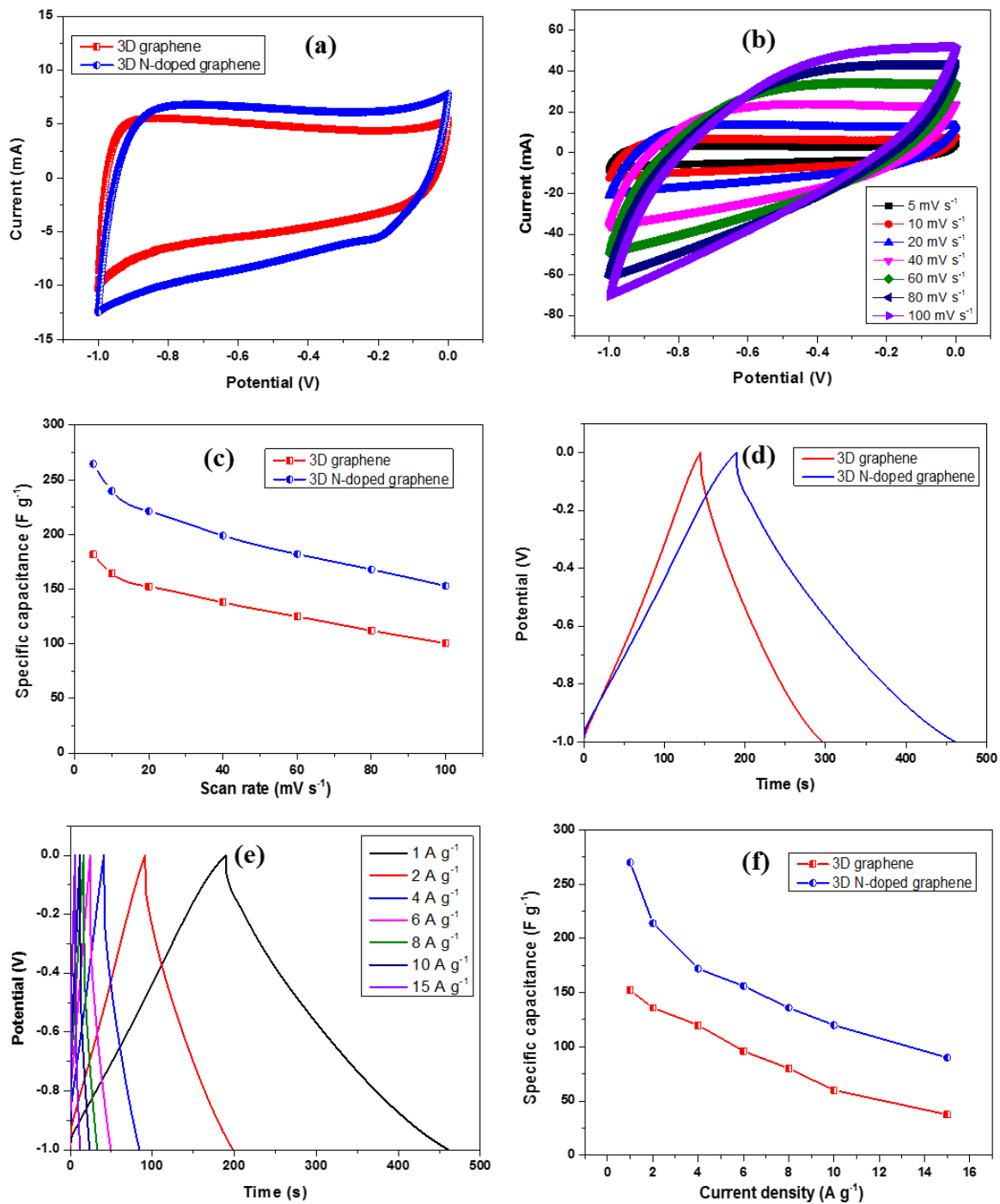


Figure. 2.4 (a) Cyclic voltammetry curves of 3DCF and 3dNCF at the scan rate of 10 mV s⁻¹ in 6M KOH solution. (b) CV curves of 3D NCF electrode at a variety of scan rates from 5 to 100 mV s⁻¹. (c) specific capacitance as a function of scan rate. (d) Galvanostatic charge/discharge plots of 3DCF and 3dNCF at a current density of 1 A g⁻¹. (e) GCD curves of 3DNCF electrode measured at various current densities from 1 to 15 A g⁻¹. (f) Specific capacitance change as a function of current density.

The electrochemical performance of the as-prepared electrode was examined by galvanostatic charge/discharge test. Figure 2.4d shows the comparative GCD curves of 3dCF and 3DNCF at the charge-discharge current density of 1 A g^{-1} . The triangular and linear shape of the GCD curves demonstrate the typical EDLC behavior and better electrochemical reversibility of the electrode materials. Apparently, the discharge time of 3DNCF was much higher than that of 3dCF, which confirmed a higher capacitance of nitrogen. The GCD performance of 3dNCF electrode was measured at different current densities. As shown in Figure 2.4e, the linear and symmetric shape of all charge-discharge curves signifies a good capacitive performance of electrode from EDLC. The calculated specific capacitance of as-prepared samples based on equation (2) is shown in Figure 2.4f. The specific capacitance values of 3DCF and 3dNCF electrode are calculated to be 152 and 270 F g^{-1} , respectively at a current density of 1 A g^{-1} . When the current density reaches to 15 A g^{-1} , a capacitance of 90 F g^{-1} can still be retained for 3DNCF, which confirms that the electrode has the good rate capability. As expected, the 3DNCF delivered higher capacitance than the as prepared 3dCF electrode. Also, the obtained specific capacitance value is higher and comparable to the previously reported nitrogen doped carbons.^{3, 18-26} Details of the comparison of our result with previously reported N-doped carbon electrode is reported in Table 2. 2.

The enhanced electrochemical performance of 3DNCF electrode can be attributed to the synergetic effect of 3D architecture, appropriate N doping, large surface area, high porosity and reasonable graphitization. The advantages of 3DNCF is as follows: (i) The 3D porous structure facilitate the effective ion migration in to the electroactive sites (short diffusion distance), thereby fast charge/discharge rate and high power density can be obtained. (ii) The 3DNCF with highly porous structure ensure the high surface area of electrochemical active sites for adsorbing ions (utilization of maximum active material) and accelerates electron transfer. (iii) The nitrogen doping could reduce the inner resistance of the carbon foams (in turn higher conductivity)^{16h, 17}, and ensure the fast electron transfer through electroactive materials to enhance the capacitive performance at high current density charge/discharge process and (iv) The surface defects and disordered morphology induced by introducing N atoms could greatly improves the wettability²⁶ of the carbon foams in the aqueous electrolyte solution and then finally leads to the enhanced electrochemical performance.

Synthesis method	Nitrogen content	Specific capacitance (F g ⁻¹)	Electrolyte	Cyclic stability (capacitance retention %)	Ref.
Hydrothermal	2.77 %	99 at 0.5 A g ⁻¹	1 M KCl	-	18
Thermal treatment	20.51 wt. %	125.4 at 0.3 A g ⁻¹	1 M KOH	500 (93%)	3
Hydrothermal	7.2 at. %	144.6 at 0.2 A g ⁻¹	6 M KOH	500 (90%)	19
Hydrothermal	8.62 at. %	148 at 1 A g ⁻¹	6 M KOH		20
Hydrothermal	2.7 %	182 at 0.5 A g ⁻¹	1 M KCl		21
Solid microwave	7.34 wt. %	197 at 0.5 A g ⁻¹	6 M KOH	5000 (98%)	22
Low temperature approach	8 at. %	217 at 1 A g ⁻¹	6 M KOH	500 (88%)	23
Ammonia flame	3.97 at. %	246.4 at 1 A g ⁻¹	6 M KOH	2000 (89.6%)	24
Hydrothermal	5.86 at. %	326 at 1 A g ⁻¹	6 M KOH	1200 (92%)	25
	3.95 at. %	266 at 1 A g ⁻¹	6 M KOH	-	
Hydrothermal	10.13 at. %	~270 at 1 A g ⁻¹	6 M KOH	2000 (~100)	26
CVD pyrolysis	4.08 %	270 at 1 A g ⁻¹	6 M KOH	5000 (~100)	This work

Table. 2.2 Comparison of the electrochemical performance of the as-prepared 3dNCF with previously reported N-doped carbon materials.

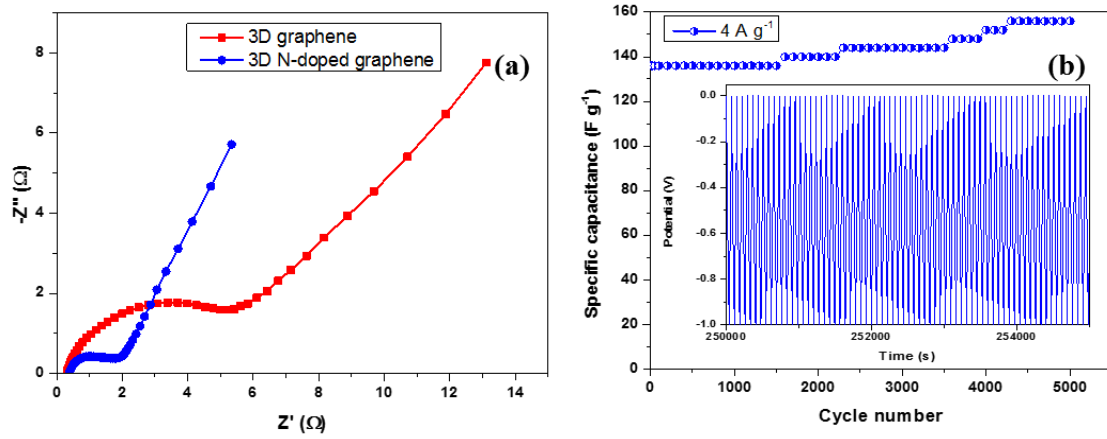


Figure. 2.5 (a) Nyquist plot of 3DNCF electrode in 6 M KOH electrolyte solution. (b) Cyclic stability of 3DNCF electrode as a function of cycle numbers. The inset shows the GCD curves at constant current of $4 A g^{-1}$.

Furthermore, the kinetic features of ion diffusion was examined by electrochemical impedance spectroscopy (EIS). The Nyquist plot of the 3DCF and 3DNCF electrode is shown in Figure. 2.5a. The plots consist of a semicircle arc at high- and medium-frequency regions and a straight line at low-frequency region. In the high frequency region, the intercept of the curve with the real axis indicates the internal resistance (R_s or ESR) of the electrode materials and electrolyte, which was found to be 0.35 and 0.39 ohm for 3dCF and 3dNCF, respectively. The diameter of the semicircular arc at the mid-frequency region corresponds to the charge transfer resistance (R_{ct}), which is caused by the charge transfer reaction at the interface of electrode and electrolyte. The 3DNCF electrode showed small R_{ct} (1.41 ohm) compared to 3dCF electrode (4.95 ohm), which suggests the better electrical conductivity of 3dNCF due to the introduction of appropriate amount N into the carbon structures. Besides the charge transfer resistance, the straight line at the low frequency region indicates the ideal capacitive behavior, which is demonstrative of ion diffusion in the electrode/electrolyte interface³. A more vertical line towards the y-axis indicates a more ideal supercapacitor behavior confirming the fast electrical double layer forming due to the low diffusion resistance of ions the structure of the electrode³. This may be due to the highly porous 3D structure, which offers better accessibility of the ions from the electrolyte. The long-term cycling stability is one of the most important electrochemical parameter for the real application of supercapacitors. The cycling stability of as-prepared 3DNCF electrodes was evaluated by the repeated GCD measurement at a constant current density of 4 A g⁻¹ for 5000 cycles. As shown in Figure. 2.5b, the 3DNCF electrode exhibits excellent cycling stability. It could be found that the specific capacitance value increases gradually up to 156 F g⁻¹ and nearly no decrease in the course of 5000 cycles (high capacitance retention), demonstrating the excellent cyclic stability. The increase in capacitance might be due to the full activation process of the electroactive materials during the long cycling process. The inset is the charge/discharge cycling curves of the 3DNCF electrode at 4 A g⁻¹. It could be clearly observed that the GCD curves exhibit a linear and symmetric in shape for all cycles indicating the EDLC behavior and good cycling stability of the 3DNCF electrodes.

Moreover, to evaluate the reliable electrochemical performance of the 3DNCF, a symmetric two-electrode cell was assembled by using 3DNCF as positive and negative electrodes in 6 M KOH solution in order to characterize the energy storage capability. Figure 2.6a shows the CV graphs of the symmetric cell measured at various scan rates of 5 to 100 mV s⁻¹ in the potential range of 0 to 1 V. All of the CV curves show a typical rectangular shape, even at the higher scan rate of 100 mV s⁻¹, which demonstrates the ideal EDLC behavior with good rate capability of 3DNCF electrode. The specific capacitance of the symmetric cell was investigated from CV curves on the basis of the mass of the electroactive materials of the both electrodes. The calculated cell and single electrode capacitance versus scan rate is plotted in Figure 2.6b. The cell and single electrode capacitance of the symmetric cell at 5 mV s⁻¹ is about 46 and 184 F g⁻¹, which is higher than the previous reported N-doped graphene material (28 F g⁻¹ at 5 mV

s^{-1})^{16d}. As the scan rate increases, the specific capacitance decreases, which is induced by the access of electrolyte ions only at the outer surface of the 3dNCF. The inner surface of the 3dNCF is inaccessible at higher scan rates due to the insufficient time available for ion diffusion and adsorption/desorption process inside the small pores (diffusion limitation at higher scan rate). However, at a scan rate of 100 mV s^{-1} , 76.7% of specific capacitance can be retained, which demonstrates the better rate capability of the cell.

The galvanostatic charge discharge (GCD) measurement was carried out to evaluate the performance of the symmetric cell at various current densities. Figure 2.6c presents the GCD curves of the 3dNCF//3dNCF symmetric cell at different current densities. The reversibility and EDLC behavior of the 3dNCF is confirmed by the linear and symmetrical charge/discharge curves. The specific capacitance of the symmetric cell can also be determined from the GCD curves on the basis of equation (2) & (3). Figure 2.6d shows the calculated cell and single electrode capacitance as a function of current density. The measured capacitance of the cell and the single electrode of the symmetric cell are found to be 37 F g^{-1} and 148 F g^{-1} at a constant current density of 0.5 A g^{-1} . With increasing current density value from 0.5 A g^{-1} to 15 A g^{-1} , the symmetric cell retained a 67% of specific capacitance indicating its good high-rate performance.

Furthermore, the cycling stability of the symmetric supercapacitor cell was tested by consecutive GCD cycling at a constant current density of 2 A g^{-1} for 10,000 cycles and the results is displayed in Figure. 2.7a. The 3DNCF //3DNCF supercapacitor exhibited an outstanding specific capacitance retention of 121%, even after 10,000 cycles of repeated charge and discharge. The initial increase of specific capacitance from 100 to 126% is owing to the full activation process of 3DNCF electrode. The inset in Figure 2.7a shows an overview of the last few cycles, which further indicates a good reversibility during consecutive fast charge-discharge process of the electrode. These results suggest that the symmetric supercapacitor based on 3D N-doped graphene sample possesses good long term cycling stability and a highly reversible in the repetitive charge/discharge cycling.

To understand the electrochemical mechanism of the 3DNCF electrode based symmetric supercapacitor cell, EIS analysis was performed for before and after long-term (10,000 cycle) GCD tests (Figure. 2.7b). It could be observed that, the Nyquist plots are almost similar in the form of semicircles in the middle-frequency region and followed by a straight in the low-frequency region, further demonstrating the good stability of the symmetric cell. The diameter of the semicircle arc becomes slightly smaller after 10,000 cycles, which shows that the ion and electron transfer path is maintained well. The straight line at frequency region closely parallel to the imaginary axis also suggests the better penetration of electrolyte ions (low ion transport resistance) as well as improved electrochemical performance of the symmetric cell through the electrochemical activation process after 10,000 cycles. The energy and power density of the 3DNCF //3DNCF symmetric cell were measured

from the discharge curves using equation 4 and 5. The Ragone plot of energy and power density of the symmetric supercapacitor at various current densities are displayed in Figure. 2.7c. The 3DNCF // 3DNCF symmetric cell exhibited a maximum energy density of 5.13 Wh Kg⁻¹ at 250 W Kg⁻¹ and a maximum power density of 7500 W Kg⁻¹ at 3.43 Wh Kg⁻¹, which suggests that the cell has great potential for practical applications.

2.4 Conclusions

In conclusion, we fabricated the 3D graphitic porous carbon structures with various porosity from various carbon precursors such as starch and PVP. The different chemical compositions and porous structures were examined by the Raman analysis, XPS, and BET surface area analysis. The PVP derived carbon foam (3dNCF) with desirable nitrogen content and porosity exhibited the outstanding electrical double layer capacitance up to 270 F g⁻¹ at 1 A g⁻¹. Energy density was estimated to be as high as 5.13 Wh Kg⁻¹ and the maximum power density reached 7.5 Kw kg⁻¹. Our fabrication strategy offers a straightforward way to develop promising candidate for electrical double layer capacitor electrode.

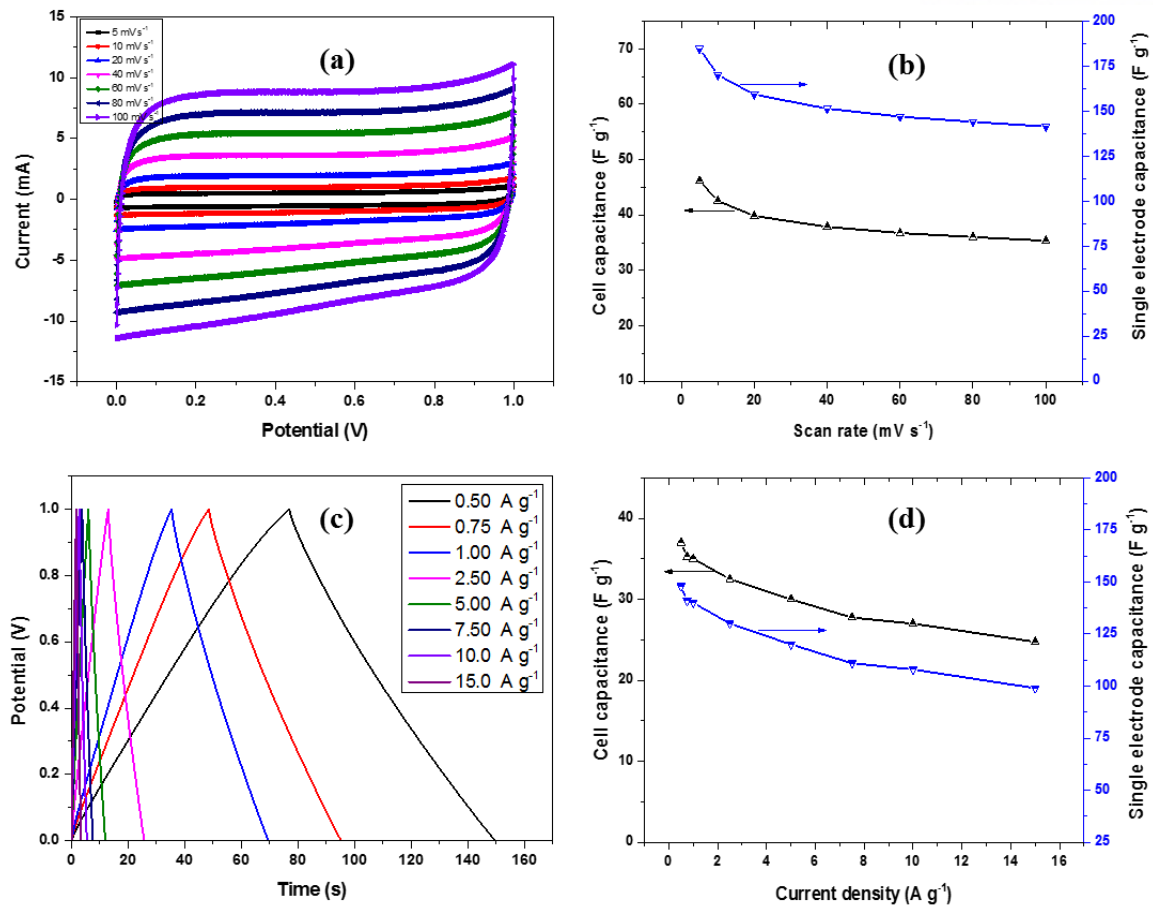


Figure. 2.6 (a) Cyclic voltammograms of 3DNCF-based symmetric supercapacitor at different scan rates. (b) Specific capacitance versus scan rates. (c) Galvanostatic charge/discharge curves of symmetric supercapacitor at different current densities. (d) Specific capacitance of symmetric supercapacitor based on total mass of active materials in two electrodes versus current density.

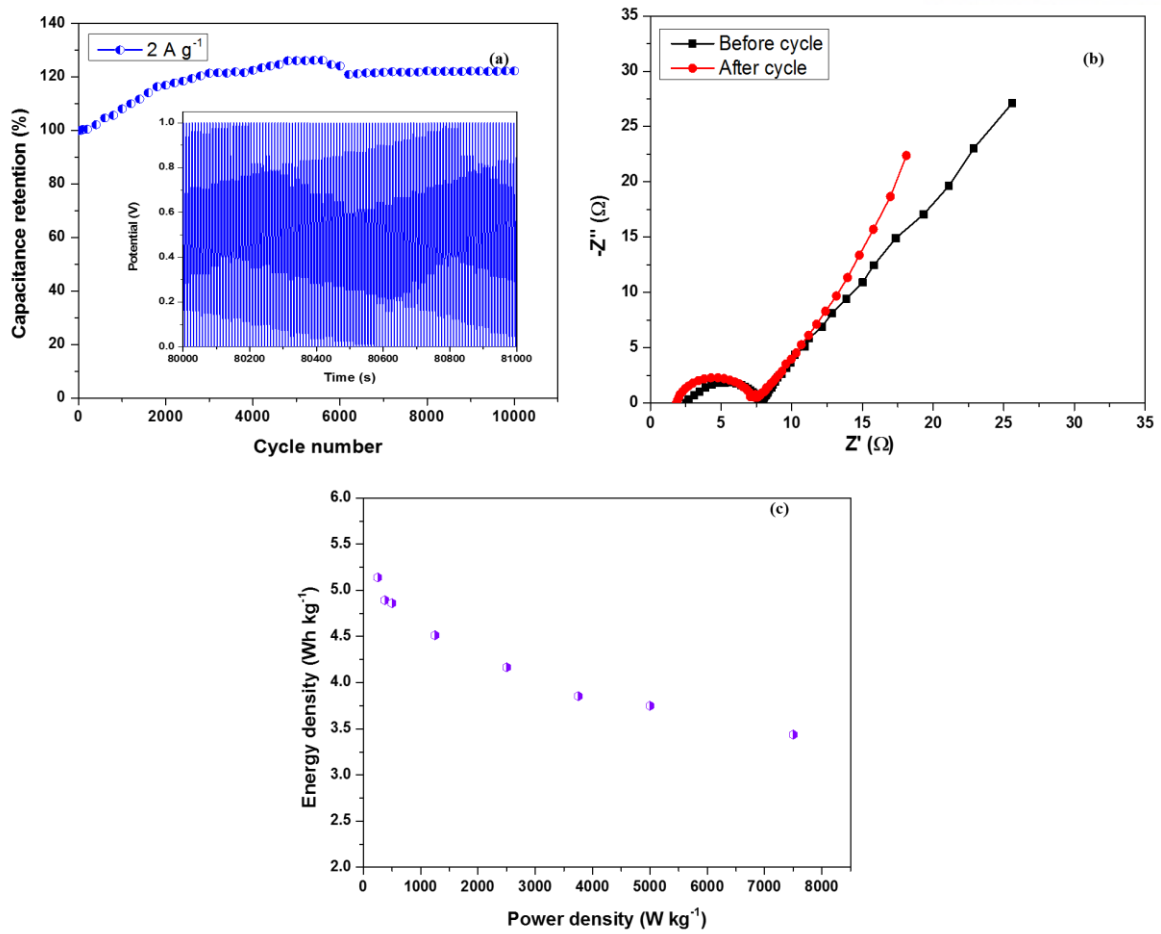


Figure. 2.7 (a) Cycling performance of 3D NNCF symmetric supercapacitor at constant current density of 2 A g^{-1} for 10000 cycles. The inset shows the GCD curves. (b) Nyquist plots of symmetric supercapacitor before and after stability test. (c) Energy density versus power density of 3DNNCF symmetric supercapacitor.

2.5. Reference:

1. Hassan, F. M.; Chabot, V.; Li, J.; Kim, B. K.; Ricardez-Sandoval, L.; Yu, A., Pyrrolic-structure enriched nitrogen doped graphene for highly efficient next generation supercapacitors. *Journal of Materials Chemistry A* **2013**, *1* (8), 2904.
2. Zhou, J.; Lian, J.; Hou, L.; Zhang, J.; Gou, H.; Xia, M.; Zhao, Y.; Strobel, T. A.; Tao, L.; Gao, F., Ultrahigh volumetric capacitance and cyclic stability of fluorine and nitrogen co-doped carbon microspheres. *Nature communications* **2015**, *6*, 8503.
3. Wang, Y.; Shi, Z.; Huang, Y.; Ma, Y.; Wang, C.; Chen, M.; Chen, Y., Supercapacitor Devices Based on Graphene Materials. *The Journal of Physical Chemistry C* **2009**, *113* (30), 13103-13107.
4. Yoon, J.-C.; Lee, J.-S.; Kim, S.-I.; Kim, K.-H.; Jang, J.-H., Three-dimensional graphene nano-networks with high quality and mass production capability via precursor-assisted chemical vapor deposition. *Scientific reports* **2013**, *3*.
5. (a) Sun, D.; Yan, X.; Lang, J.; Xue, Q., High performance supercapacitor electrode based on graphene paper via flame-induced reduction of graphene oxide paper. *Journal of Power Sources* **2013**, *222*, 52-58; (b) Ramadoss, A.; Saravanakumar, B.; Kim, S. J., Thermally reduced graphene oxide-coated fabrics for flexible supercapacitors and self-powered systems. *Nano Energy* **2015**, *15*, 587-597; (c) Balasingam, S. K.; Lee, J. S.; Jun, Y., Few-layered MoSe₂ nanosheets as an advanced electrode material for supercapacitors. *Dalton Transactions* **2015**, *44* (35), 15491-15498.
6. Hou, J.; Cao, C.; Idrees, F.; Ma, X., Hierarchical Porous Nitrogen-Doped Carbon Nanosheets Derived from Silk for Ultrahigh-Capacity Battery Anodes and Supercapacitors. *ACS nano* **2015**, *9* (3), 2556-2564.
7. Ferrari, A.; Meyer, J.; Scardaci, V.; Casiraghi, C.; Lazzeri, M.; Mauri, F.; Piscanec, S.; Jiang, D.; Novoselov, K.; Roth, S., Raman spectrum of graphene and graphene layers. *Physical review letters* **2006**, *97* (18), 187401.
8. Wei, W.; Liang, H.; Parvez, K.; Zhuang, X.; Feng, X.; Mullen, K., Nitrogen-doped carbon nanosheets with size-defined mesopores as highly efficient metal-free catalyst for the oxygen reduction reaction. *Angewandte Chemie* **2014**, *53* (6), 1570-4.
9. Zhang, J.; Zhao, Z.; Xia, Z.; Dai, L., A metal-free bifunctional electrocatalyst for oxygen reduction and oxygen evolution reactions. *Nature nanotechnology* **2015**, *10* (5), 444-52.
10. Qie, L.; Chen, W. M.; Wang, Z. H.; Shao, Q. G.; Li, X.; Yuan, L. X.; Hu, X. L.; Zhang, W. X.; Huang, Y. H., Nitrogen-Doped Porous Carbon Nanofiber Webs as Anodes for Lithium Ion Batteries with a Superhigh Capacity and Rate Capability. *Advanced materials* **2012**, *24* (15), 2047-2050.
11. Qie, L.; Chen, W.; Xu, H.; Xiong, X.; Jiang, Y.; Zou, F.; Hu, X.; Xin, Y.; Zhang, Z.; Huang, Y., Synthesis of functionalized 3D hierarchical porous carbon for high-performance supercapacitors. *Energy & Environmental Science* **2013**, *6* (8), 2497-2504.

12. Dutta, S.; Bhaumik, A.; Wu, K. C.-W., Hierarchically porous carbon derived from polymers and biomass: effect of interconnected pores on energy applications. *Energy & Environmental Science* **2014**, 7 (11), 3574-3592.
13. Morant, C.; Andrey, J.; Prieto, P.; Mendiola, D.; Sanz, J.; Elizalde, E., XPS characterization of nitrogen-doped carbon nanotubes. *physica status solidi (a)* **2006**, 203 (6), 1069-1075.
14. Li, Z.; Xu, Z.; Tan, X.; Wang, H.; Holt, C. M.; Stephenson, T.; Olsen, B. C.; Mitlin, D., Mesoporous nitrogen-rich carbons derived from protein for ultra-high capacity battery anodes and supercapacitors. *Energy & Environmental Science* **2013**, 6 (3), 871-878.
15. C. Xu, J. Sun, L. Gao, Synthesis of novel hierarchical graphene/polypyrrole nanosheet composites and their superior electrochemical performance, *Journal of Materials Chemistry*, 21 (2011) 11253-11258.
16. Q. Zhou, X. Ye, Z. Wan, C. Jia, A three-dimensional flexible supercapacitor with enhanced performance based on lightweight, conductive graphene-cotton fabric electrode, *Journal of Power Sources*, 296 (2015) 186-196.
17. M. Lee, S.K. Balasingam, H.Y. Jeong, W.G. Hong, H.-B.-R. Lee, B.H. Kim, Y. Jun, One-step hydrothermal synthesis of graphene decorated V₂O₅ nanobelts for enhanced electrochemical energy storage, *Scientific Reports*, 5 (2015) 8151.
18. V. Chabot, F.M. Hassan, A. Yu, Nitrogen doped graphene as a high efficient electrode for next generation supercapacitors, *ECS Transactions*, 2012, pp. 19-26.
19. B. Zheng, T.-W. Chen, F.-N. Xiao, W.-J. Bao, X.-H. Xia, KOH-activated nitrogen-doped graphene by means of thermal annealing for supercapacitor, *J Solid State Electrochem*, 17 (2013) 1809-1814.
20. B. Jiang, C. Tian, L. Wang, L. Sun, C. Chen, X. Nong, Y. Qiao, H. Fu, Highly concentrated, stable nitrogen-doped graphene for supercapacitors: Simultaneous doping and reduction, *Applied Surface Science*, 258 (2012) 3438-3443.
21. J.W. Lee, J.M. Ko, J.-D. Kim, Hydrothermal preparation of nitrogen-doped graphene sheets via hexamethylenetetramine for application as supercapacitor electrodes, *Electrochimica Acta*, 85 (2012) 459-466.
22. F.M. Hassan, V. Chabot, J. Li, B.K. Kim, L. Ricardez-Sandoval, A. Yu, Pyrrolic-structure enriched nitrogen doped graphene for highly efficient next generation supercapacitors, *Journal of Materials Chemistry A*, 1 (2013) 2904-2912.
23. K. Wang, L. Li, T. Zhang, Z. Liu, Nitrogen-doped graphene for supercapacitor with long-term electrochemical stability, *Energy*, 70 (2014) 612-617.
24. B. Xie, Y. Chen, M. Yu, X. Shen, H. Lei, T. Xie, Y. Zhang, Y. Wu, Carboxyl-Assisted Synthesis of Nitrogen-Doped Graphene Sheets for Supercapacitor Applications, *Nanoscale Res Lett*, 10 (2015) 1-11.

25. D. Li, C. Yu, M. Wang, Y. Zhang, C. Pan, Synthesis of nitrogen doped graphene from graphene oxide within an ammonia flame for high performance supercapacitors, *RSC Advances*, 4 (2014) 55394-55399.
26. H.-L. Guo, P. Su, X. Kang, S.-K. Ning, Synthesis and characterization of nitrogen-doped graphene hydrogels by hydrothermal route with urea as reducing-doping agents, *Journal of Materials Chemistry A*, 1 (2013) 2248-2255.
27. L. Sun, L. Wang, C. Tian, T. Tan, Y. Xie, K. Shi, M. Li, H. Fu, Nitrogen-doped graphene with high nitrogen level via a one-step hydrothermal reaction of graphene oxide with urea for superior capacitive energy storage, *RSC Advances*, 2 (2012) 4498-4506.
28. M. Seredych, D. Hulicova-Jurcakova, G.Q. Lu, T.J. Bandosz, Surface functional groups of carbons and the effects of their chemical character, density and accessibility to ions on electrochemical performance, *Carbon*, 46 (2008) 1475-1488.
29. T. Kwon, H. Nishihara, H. Itoi, Q.-H. Yang, T. Kyotani, Enhancement Mechanism of Electrochemical Capacitance in Nitrogen-/Boron-Doped Carbons with Uniform Straight Nanochannels, *Langmuir*, 25 (2009) 11961-11968.

Chapter 3. Hierarchical porous nitrogen-doped graphitic carbon foam with 3-Dimensional networks as highly active oxygen catalyst for Zn-air battery

3.1. Introduction

Rechargeable metal-air batteries have been widely attracted on as a possible alternatives to meet the increasing requirements for energy resources and growing environmental concerns especially due to its high energy densities, low cost, abundance, eco-friendly¹. In the metal-air cells, diffused oxygen molecules are reduced at air electrode during discharging, and the reverse reaction including oxygen evolution occurs during charging. One of the major issues of zinc-air battery technologies facing now is to develop the efficient, robust air catalysts with high cycle stability for oxygen reduction reaction (ORR) and oxygen evolution reaction (OER), possibly working in aqueous electrolytes^{2,3}. So far, precious metals and its alloy based nanomaterials such as platinum, ruthenium and iridium have been investigated as such electrocatalyst⁴. However, their high price and poor durability retard the wide commercialization of the Zn-air battery technology. In this regard, lots of efforts to develop efficient, low cost and durable candidates for such noble metal based catalysts by applying nonprecious metal based catalysts^{5,6} or metal-free carbonaceous materials^{7,8}.

Heteroatom-doped (B, S, N, P, Cl, and I) carbon nanomaterials have been reported as a promising catalysts exhibiting excellent ORR activity in alkaline aqueous electrolyte^{9,10}. Introduction of heteroatoms into graphitic structure modifies the electronic structure and catalytic sites, the adsorption and breakage energy of O₂, and the reaction mechanism of catalysts, thereby dramatically facilitate the ORR performances¹¹. Nitrogen doped carbon materials (NCMs) have been the most attractive catalysts for the ORR because nitrogen atoms lead to high electrochemical activity as well as possess other desirable features such as high surface areas, long-term stability, and outstanding resistance to methanol cross-over effects for the ORR in an alkaline medium^{12,13}. NCMs have been fabricated by employing thermal treatment of carbon sources with nitrogen containing reactive gases such as ammonia or acetonitrile¹⁴, thermolysis of polymers containing nitrogen⁷. The direct pyrolysis of nitrogen-containing hydrocarbons or polymers are reported to produce nitrogen-doped carbon materials with good incorporation of nitrogen with avoidably involving the use of toxic gases¹⁵. Furthermore, as it well reported, the three-dimensional hierarchical porous carbon materials with large volumetric surface area and interconnected network structures for a high density of catalytic active site and efficient mass transport hence guarantee enhanced ORR activity¹⁶ have been developed with a variety of approaches including hard template assisted synthesis¹⁷, post-activation fabrication⁷, and direct pyrolysis of polymer aerogels¹⁸.

Herein, we developed a three-dimensional nitrogen-doped graphitic carbon foam (3dNCF) with large specific surface area ($\sim 1509 \text{ m}^2 \text{ g}^{-1}$) which shows outstanding electrocatalytic performance for

both ORR and OER. The 3dNCFs were from Poly vinyl pyrrolidone (PVP) and iron (III) chloride as a nitrogen-enriched carbon source and metal catalysts precursor, respectively. The direct pyrolysis of nitrogen containing precursors promise an increased active site density with a well-distributed nitrogen atoms on the carbon surface¹⁹. Moreover, the reduced iron frames and particles from iron salt (FeCl_3) affect the graphitization of the catalysts²⁰ as well as generate pores after leaching process²¹. The resultant 3dNCFs with the hierarchical architectures and abundant heteroatom doped active sites show outstanding ORR properties with a relatively positive half wave potential of $-0.113 \text{ V vs Ag/AgCl}$, high selectivity, remarkable resistance to methanol, and superior cycling stability in an alkaline medium. Moreover, the 3dNCF catalyst pronounced the OER performances in alkaline medium and excellent ORR performances even in acidic medium, which make the 3dNCF catalysts powerful oxygen catalysts.

3.2. Experimental Section

3.2.1. Synthesis

The optimized amount of poly vinyl pyrrolidone (PVP, Mw = 40,000, Sigma Aldrich) was dissolved in D.I. water at room temperature and then mixed with the suitable amount of $\text{FeCl}_3 \cdot 6\text{H}_2\text{O}$. The prepared solution was coated onto the prepared SiO_2 template to make the $\text{SiO}_2/\text{PVP}/\text{FeCl}_3$ composites. The prepared composites were dried in a vacuum oven at room temperature, followed by thermolysis at targeted temperature for 30 minutes under hydrogen / argon mixed atmosphere. The acid washing proceeds to remove the sacrificial SiO_2 template and iron simultaneously.

3.2.2. Characterization

Field-Emission Scanning Electron Microscopy (FESEM) was performed on Hitachi S-4800. Transmission electron microscope (TEM) images were collected on JEM-2100 (JEOL, Japan). High-resolution TEM (HRTEM) and EDS mapping were performed using a JEM-2100F (JEOL). Thermogravimetric analysis (TGA) measurements were conducted on Q500 (TA instruments) under argon flow with a ramping rate of $15^\circ\text{C min}^{-1}$. Nitrogen adsorption-desorption isotherms were measured using an ASAP 2020 instrument (Micromeritics) at 77 K using Barrett-Emmett-Teller (BET) calculations for the surface area. The pore size distribution was calculated on the basis of the Barrett-Joyner-Halenda (BJH) model. X-ray photoelectron spectra (XPS) were performed on K-alpha X-ray photoelectron spectrometer (ThermoFisher). Fourier transform infrared spectra (FT-IR) were measured on a Cary 670 FTIR (Agilent Technology). The Raman spectra were recorded with the alpha300R spectrometer (WITec) using 532 nm laser.

3.2.3 Electrochemical Measurements

The electrocatalytic activity of the catalysts were investigated by using a RDE system on a VMP3 biologic electrochemical potentiostat. A traditional three-electrode cell with a platinum wire as the counter electrode and a saturated silver-silver chloride (Ag/AgCl) electrode as the reference electrode. The working electrodes was prepared as follow: the prepared sample (10 mg) was dispersed in a aqueous solution of 450 ul of ethanol and 50 ul of Nafion (5 wt%) to form a homogeneous ink by sonication for 1 h. The prepared 3.75 ul of suspension was pipetted on the surface of pre-polished glassy carbon electrode (5 mm in diameter), which was dried by rotating evaporation²² at room temperature to form a thin film of catalyst layer. Commercial Pt/C (20 wt%, Premetek) was also tested for comparison. Pt/C ink was prepared as follows 5 mg Pt/C and 10 ul Nafion (5 wt%) was dispersed in 1.99 ml H₂O and 0.5 ml IPA stock solution and sonicated to obtain a well dispersed suspension. 6.25 ul of Pt/C catalyst suspension was then dropped on the glassy carbon electrode, resulting in a targeted catalyst loading of 0.1 mg cm⁻² (20 ug_{pt} cm⁻²). RDE and RRDE measurements were conducted in N₂- and O₂-saturated 0.1 M KOH, 0.5 M H₂SO₄, and 0.1 M HClO₄ electrolytes, respectively hence subtract the background capacitive current. The CV tests were measured at a scan rate of 50 mVs⁻¹ and the RDE tests were examined in the purged electrolytes at a scan rate of 10 mVs⁻¹ with a variety of electrode rotating speeds. The chronoamperometric responses were measured at -0.25 V in O₂-saturaed 0.1 M KOH at 1600 rpm. For methanol crossover test, 3M of methanol was injected by using microsyringe. The electron transfer number (n) was investigated from RRDE tests based on the disk current (I_D), ring current (I_R), and the current collection efficiency of Pt ring (N) by the following equations:

$$n = 4 \times \frac{I_D}{I_R/N + I_D}$$

The peroxide percentage (H₂O₂ %) was evaluated from the following equation:

$$H_2O_2 \% = 200 \times \frac{I_R/N}{I_R/N + I_D}$$

3.3. Results and Discussion

The overall synthetic procedure for the 3dNCFs is similar to the method we already reported. Briefly, the 3dNCF is fabricated via the combination of nitrogen-enriched polymers, iron salts, and fumed silica templates. Fumed silica with an aggregated diameter of 200 nm to 300 nm were initially self-assembled to form closed-packed silica template and the aqueous PVP precursor solution mixed with a targeted amount of FeCl_3 homogeneously coated onto the silica template. After vacuum drying to remove water, the subsequent thermal treatment of PVP/ FeCl_3 coated silica in hydrogen and argon mixed gas flowing condition at 800, 900, and 1000°C combined with etching of silica and reduced iron nanoparticles generated 3dNCF-X where x stands for different thermal treatment temperatures. To identify how the iron salts (FeCl_3) affect the porosity, morphology, and further catalytic performance of the samples, the same procedure was carried out by employing the PVP precursor solution without iron salts and pyrolyzed at 800°C which is denoted as 3dNC-800. For comparison, 3d graphitic carbon foam was fabricated in the same way we already reported²¹.

The thermal decomposition process was studied by thermogravimetric analysis (TGA) (Figure 3.1), which confirms that most of the PVP was decomposed above to 500°C and the Fe(III) ions were reduced.²¹ The metal salts (FeCl_3) was also reported by effective activation-graphitization agents during thermal treatment process, which can produce a porous structure with sufficient micro- and mesopores for a high surface area^{20, 21}. Specifically, during the thermal treatment of PVP/ FeCl_3 precursor, gaseous carbon, nitrogen, and iron species are simultaneously formed¹⁹. Reduced iron frame and particles gradually capture carbon and nitrogen species then atoms are catalytically decomposed into carbon and nitrogen atoms, respectively, which promote conversion of amorphous carbon derived from PVP to nitrogen doped graphitic carbon fragments around the iron surface¹⁹.

A scanning electron microscopy (SEM) image (Figure 3.2a) and transmission electron microscopy (TEM) images associated with elemental mapping (Figure. 3.2 b-d) after eliminating the silica and iron particles demonstrates the uniform distribution of C, O and N on the 3D hierarchical graphitic carbon foam for a sample thermolysis at 800°C (3dNCF-800). Magnified high-resolution TEM images of 3dNCF-800 further confirm the formation of curved graphitic domains (Fig 3.2 c). The interconnected nanostructures for all the 3dNCFs (figure3.3-3.6) possess a large number of exposed graphitic networks, which play a crucial role in oxygen catalysts²³. SEM and TEM images for 3dNC-800 (Figure 3.3) were also investigated to confirm how metal salts affects the porous architecture during thermal treatment. 3dNC-800 pyrolyzed without metal salts shows the nonporous stacked sheet like structures with little graphitic edges whereas 3dNCFs show the hierarchical mesoporous structures with numerous graphitic carbon edges. As investigated by SEM and TEM, the higher porosity and graphitization of the 3dNCF than that of 3dNC can be achieved by introducing the metal salts in the PVP precursor, which indicates the hierarchical porous structures are derived from the synergetic effect of sacrificial silica template and

iron salts. So, we assume that the reduced iron species served as three-dimensional frame to give rise to the porosity of the 3dNCF as well as transition-metal catalysts for a growth of graphitic carbon.

The Raman analysis of 3dNC and 3dNCF-X shows two distinct signals around 1590 cm^{-1} and 1352 cm^{-1} , which can be associated with graphitic carbon (G peak) and disordered carbon (D Peak), respectively (Figure 3.2e)²⁴. Even though 3dNCFs has the more hierarchical porous structures than 3dNC have, their similar I_D/I_G values with the two small bumps between $2300 - 3200\text{ cm}^{-1}$ instead of well-defined second ordered peaks (2D, D+D', D+G) for all the samples reveal a similar nano-crystalline graphitic characteristic²⁵ between 3dNC-800 and 3dNCFs.

The porous characteristics for the 3dNC and 3dNCF-X were determined by N_2 isothermal adsorption/desorption measurement (Figure 3.2f) and the results with Brunauer-Emmett-Teller (BET) surface area, total pore volume are summarized (Table 3.1). Compared to the nonporous type II isotherm plots for 3dNC-800, the type IV with a sharp increase in nitrogen adsorption for 3dNCF-X at a high pressure ($P/P_0 = 0.70 - 0.99$) demonstrates the well-developed mesoporosity²⁶ generated by metal salts. The BET surface area and pore volumes of 3dNCFs were measured from 1183 to $1509\text{ m}^2\text{ g}^{-1}$ and 2.17 to $2.735\text{ cm}^3\text{ g}^{-1}$, respectively, which are much higher than that of 3dNC ($476\text{ m}^2\text{ g}^{-1}$ and $0.12\text{ cm}^3\text{ g}^{-1}$). Remarkably, as the thermal treatment temperature increases, the surface area and the pore volume of 3dNCFs significantly enhanced as listed in table 3.1, which might be due to the generated volatile gases from carbonization process of precursors¹⁸ especially the temperature below 500°C as well as the different precipitation process of carbons on the iron particles. Further research will be devoted to confirm the exact pore forming mechanisms. The pore sizes distribution based on the Barrett-Joyner-Halenda (BJH) method (Figure 3.2 g) reveals the mesoporous features with the pore diameters less than 10 nm for all 3dNCF-X samples.

As investigated, the direct pyrolysis process of PVP/metal salts with sacrificial silica templates successfully produces the hierarchical interconnected architectures with high density of nitrogen doped graphitic carbons which have high surface area, large volumetric pores with a various size distribution which is promising candidate for oxygen electrocatalysts.

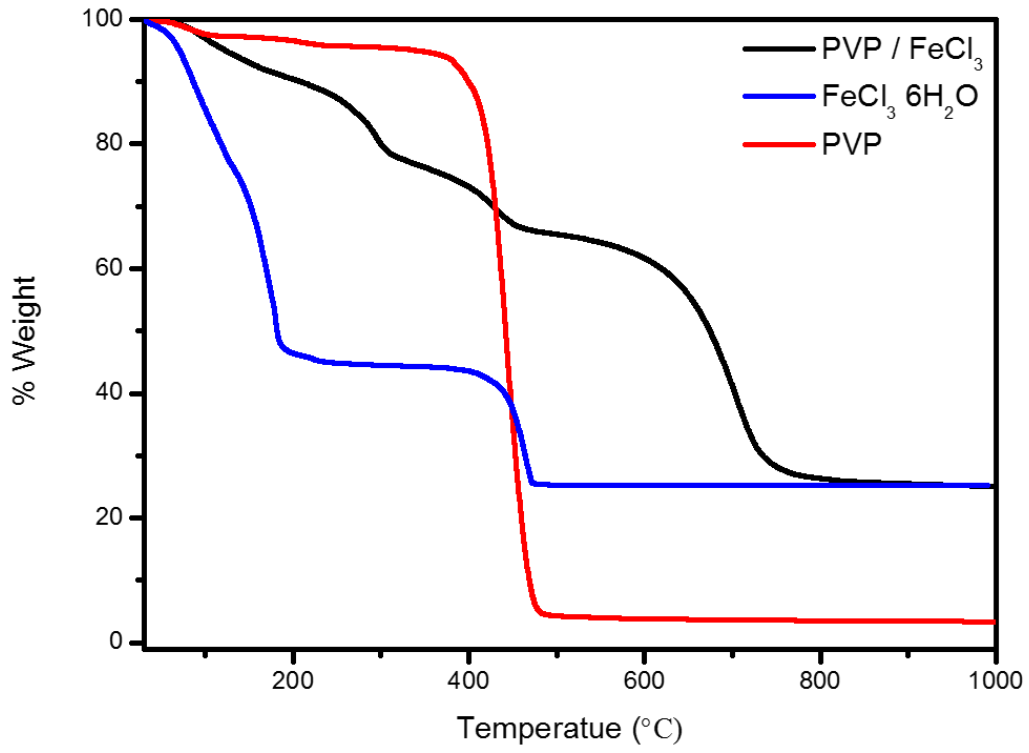


Fig. 3.1. TGA curves of PVP, FeCl₃, and PVP/FeCl₃.

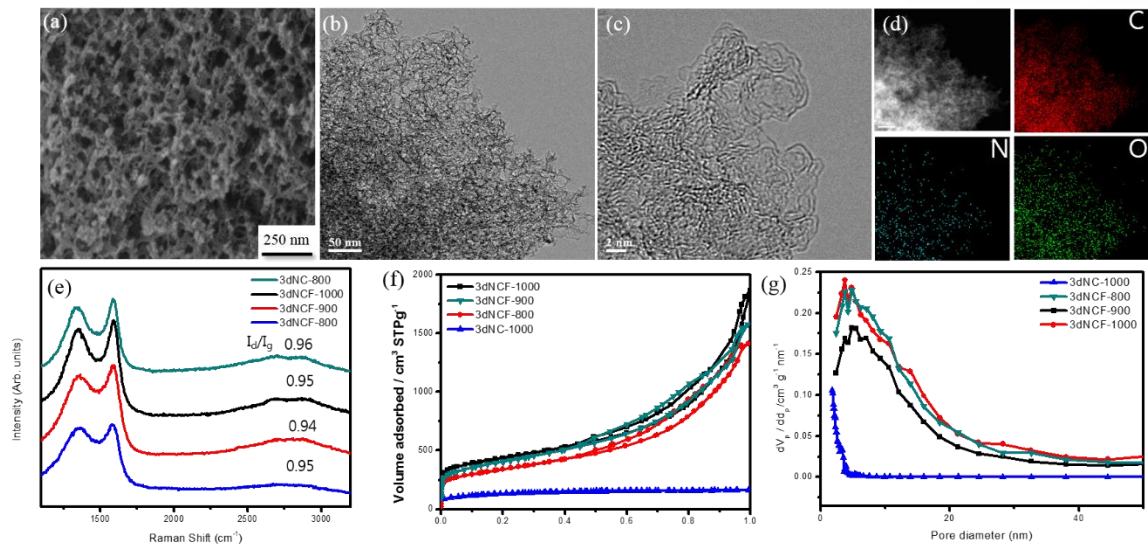


Figure 3.2. (a) SEM image of the 3dNCF. (b, c) TEM image of the 3dNCF-800. (d) TEM image of 3dNCF-800 with corresponding elemental mapping. (e) Raman spectra of 3dNC and 3dNCFs. (f) Nitrogen adsorption/desorption of the 3dNC and 3dNCFs. (g)BJH curves of 3dNC and 3dNCFs.

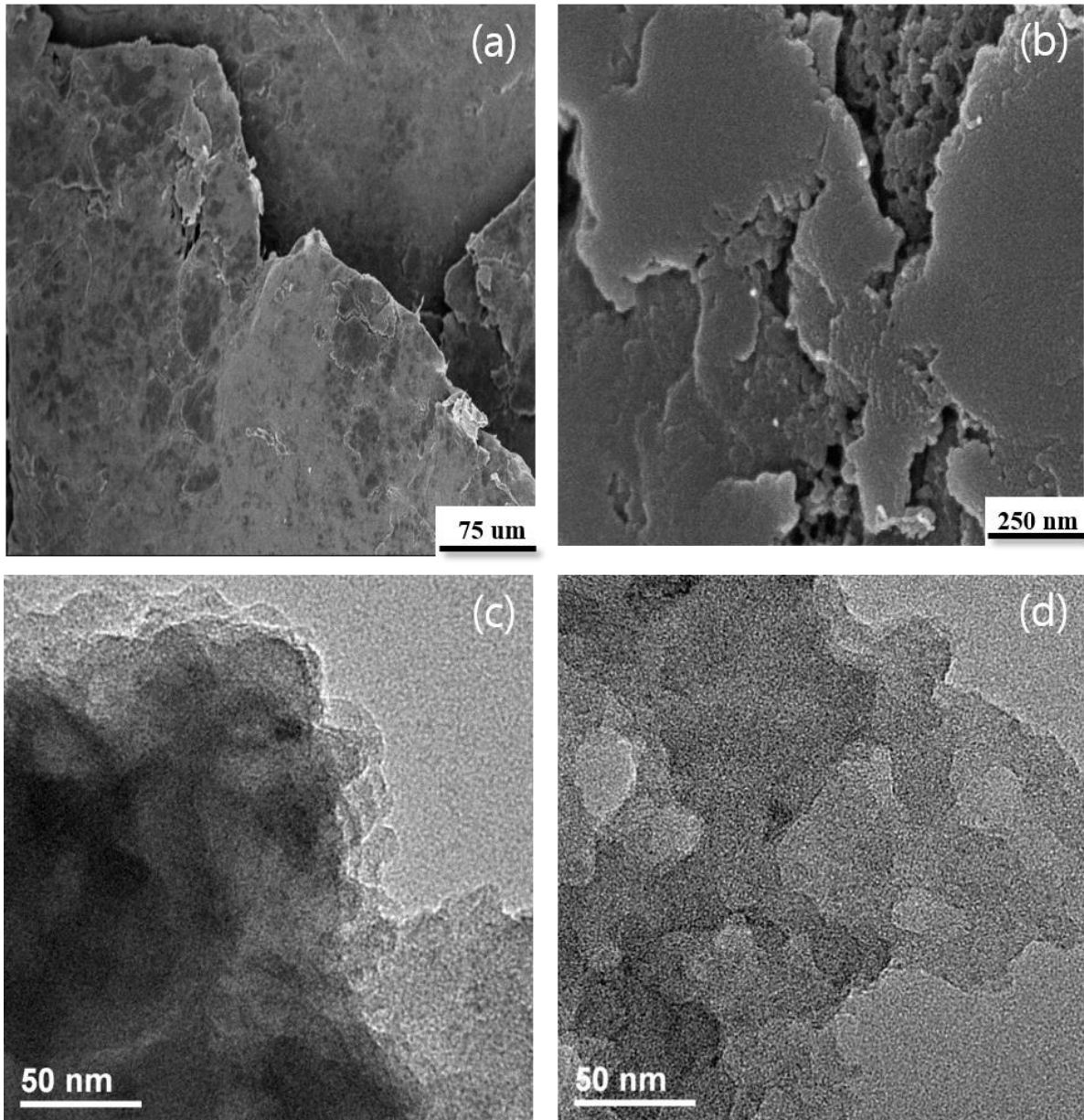


Figure 3.3 SEM and TEM images of 3dNC-800 with different magnifications.

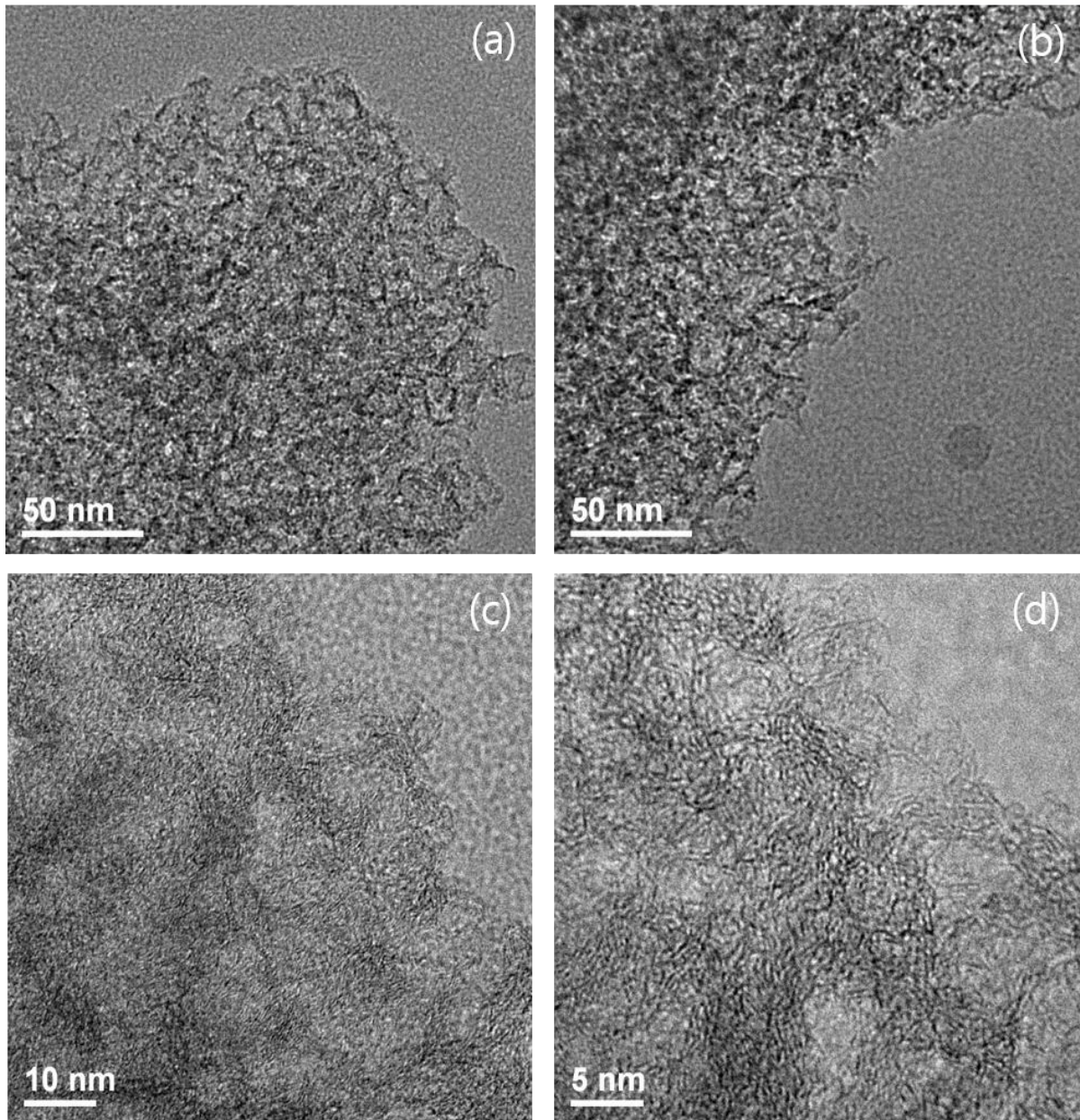


Figure 3.4. Additional TEM images of 3dNCF-800 with different magnifications

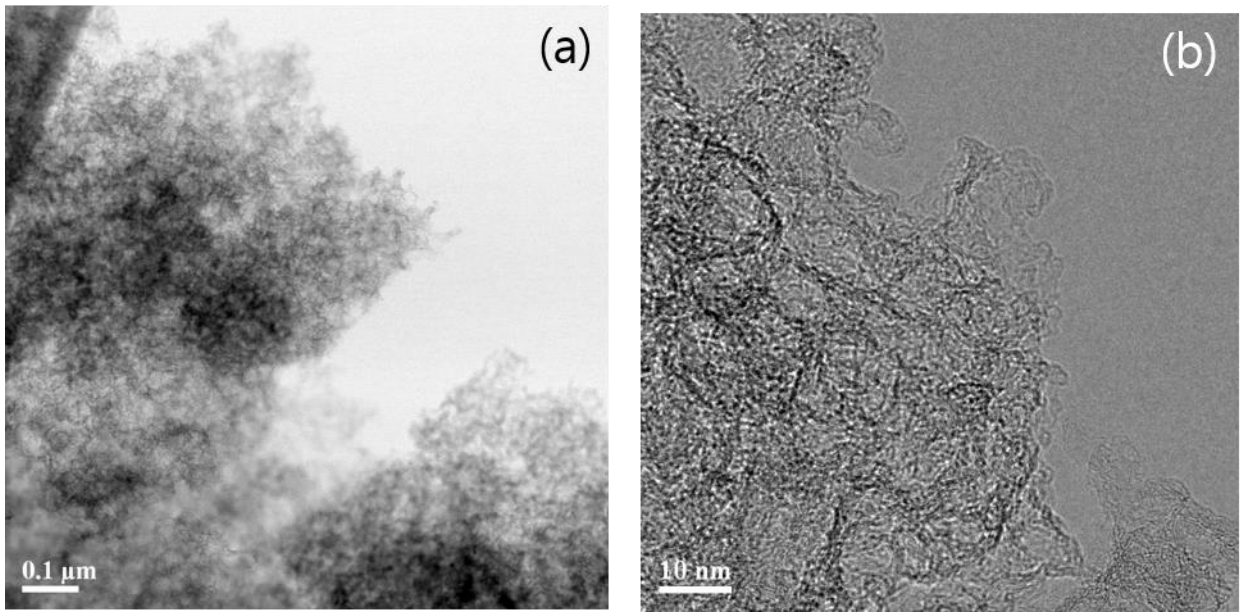


Figure 3.5. TEM images of resulting 3dNCF-900

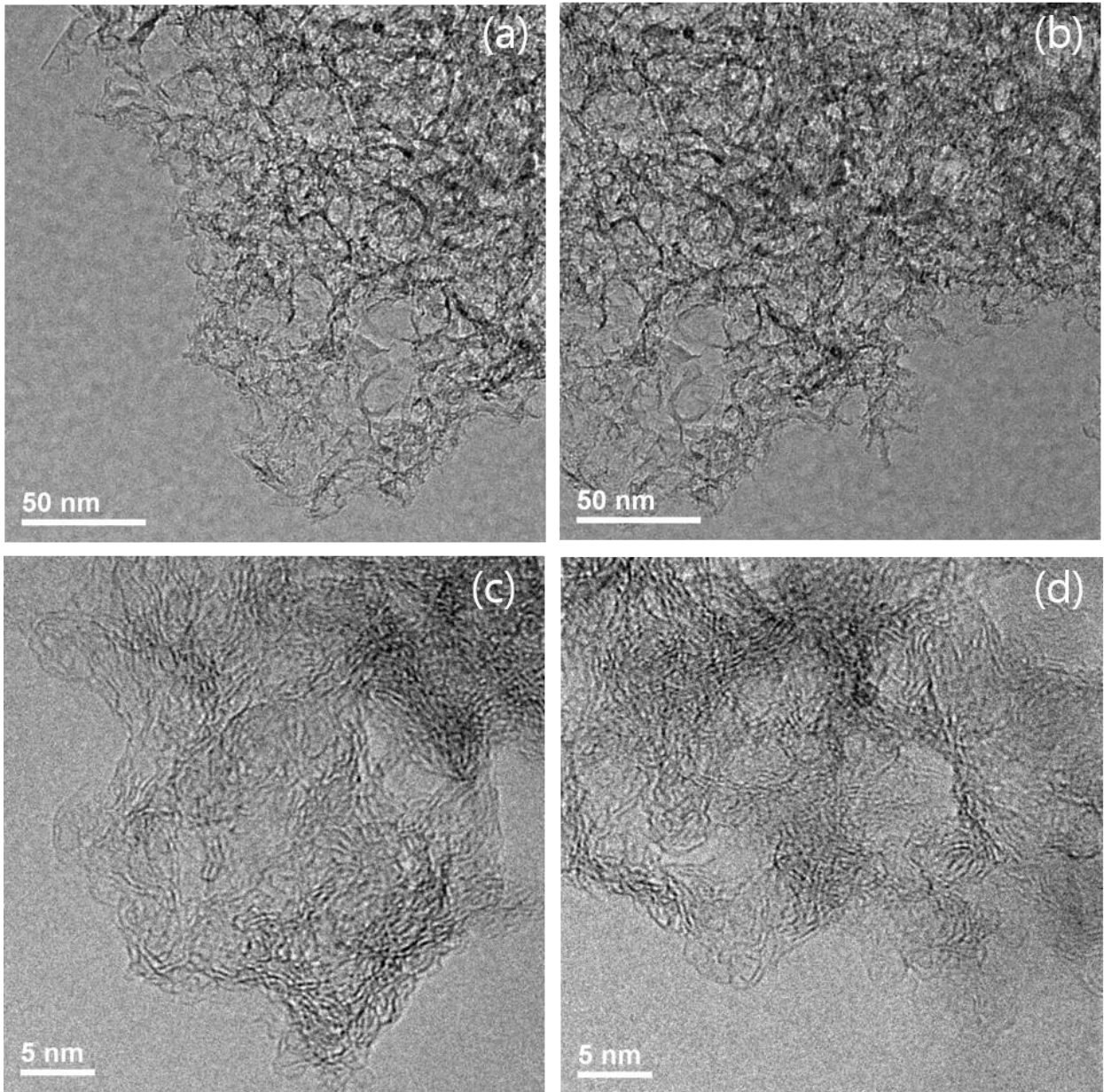


Figure 3. 6. TEM image of resulting 3dNCF-1000

	Surface area ($\text{m}^2 \text{g}^{-1}$)	Total pore volume ($P/P_0 = 0.990$) ($\text{cm}^3 \text{g}^{-1}$)	Average pore diameter (nm)
PVP only 1000°C	476	0.12	2.64
800°C	1183	2.17	7.34
900°C	1405	2.192	7.31
1000°C	1509	2.735	7.25

Table 3.1. Specific surface areas (SSA) and total pore volume and average pore diameter distribution of 3DNCs.

The chemical composition of the prepared catalysts were investigated by the X-ray photoelectron spectroscopy (XPS) measurements. The XPS survey scans confirm the existence of C, O, and N atoms demonstrating that the silica template and iron catalysts are completely removed after acid washing (Figure 3.7.) The atomic contents are summarized in Table S2. The 3dNCF-X shows a high proportion of carbon and small amount of nitrogen (3.47 – 4.45 at %) derived from the high N/C ratio of PVP precursor. Even though pyrolyzed under the same temperature, 3dNC and 3dNCF-800 exhibit different chemical composition and nitrogen species, which suggests the crucial role of the iron catalyst in thermal decomposition process of carbon precursor²⁷. The high resolution peaks for N1s of the 3dNCF-X was further deconvoluted into four peaks centered at ~398.0 eV, 399 eV, 400.7 eV and 402.6 eV corresponding to pyridinic, pyrrolic, graphitic, and oxidized nitrogen, respectively(Figure 3.8. a – d)^{28,29}.

The N1s curve fitting indicates a conversion from pyrrolidone branched polymer to nitrogen doped graphitic carbon structures. As summarized in table 3.2, thermally unstable pyridinic and pyrrolic nitrogen is converted to thermally stable graphitic nitrogen with increasing temperature, which facilitate the different chemical/electronic environments and hence electrocatalytic activities. It is critical to optimize the pyrolysis temperature to fabricate 3dNCF-X possessing the desired porosity and nitrogen contents since overheating caused a higher surface area and a carbonization degree but a gradual loss of nitrogen dopants from the carbon architecture.

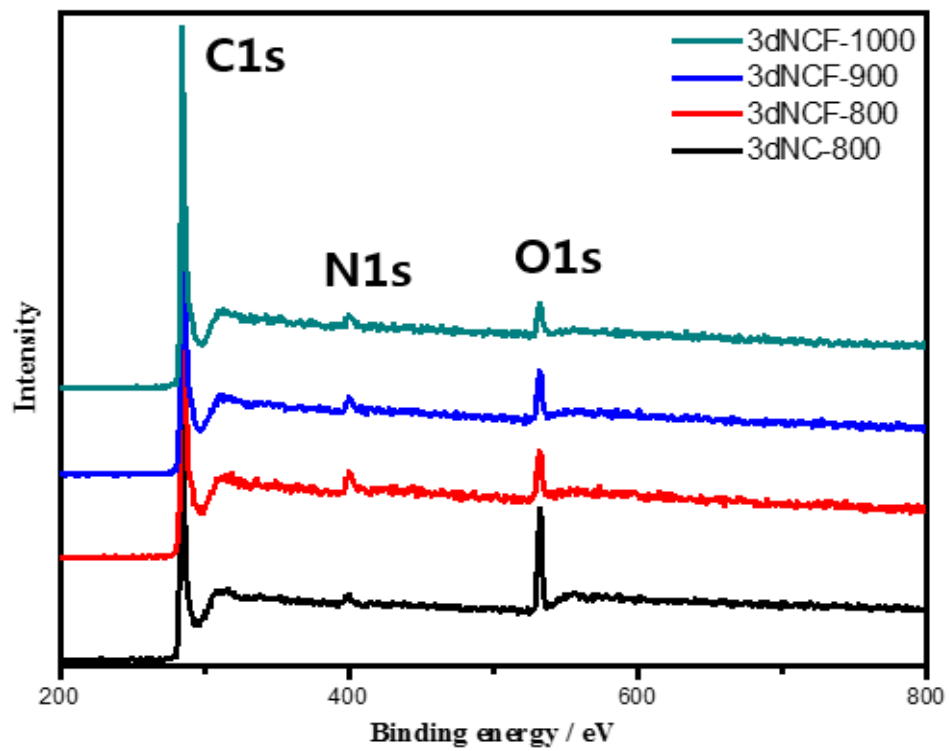


Figure 3. 7. XPS survey spectra of prepared 3dNC and 3dNCF-Xs.

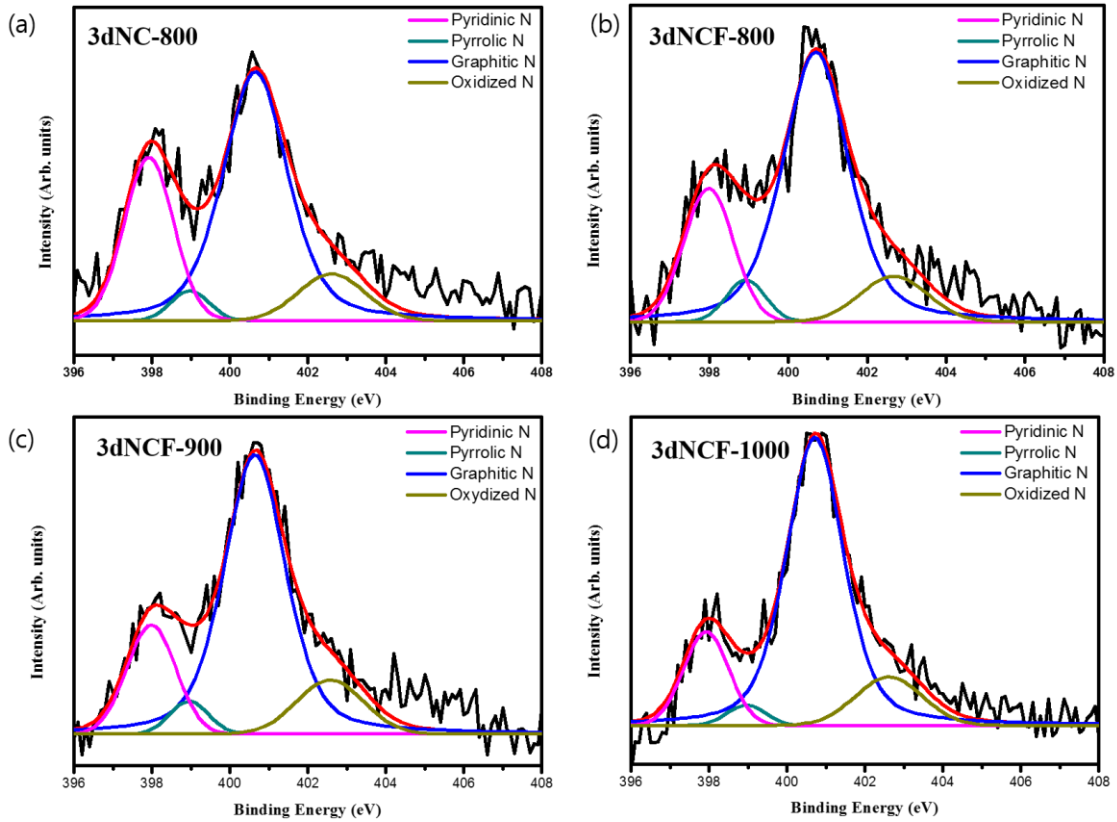


Figure 3. 8. High-resolution N1s XPS signals for 3dNC-800 (a), 3dNCF-800 (b), 3dNCF-9000 (c), and 3dNCF-1000 (d). The signals deconvoluted into four energy components around 398.0, 398.9, 400.7, and 402.7 eV, indicating the presence of pyridinic-, pyrrolic-, graphitic- and oxidized-N, respectively.

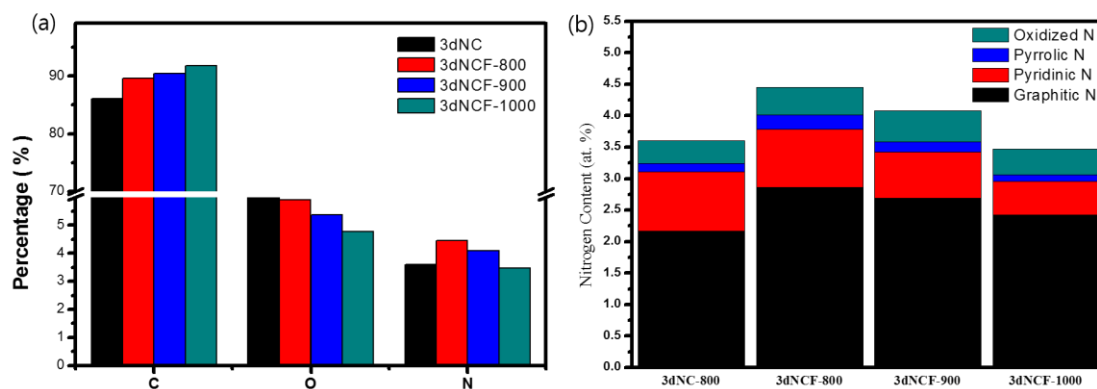


Figure. 3.9 (a) Atomic content of 3dNC and 3dNCF-X. (b) Atomic contents of pyridinic N, pyrrolic N, graphitic N, and oxidized N calculated in N1s XPS spectra.

Catalysts	C (at. %)	N (at. %)	O (at. %)	Pyridinic N (at. %)	Pyrrolic N (at. %)	Graphitic N (at. %)	Oxidized N (at. %)
3dNC-800	86.05	3.61	10.23	26.15	3.71	60.08	10.05
3dNCF-800	89.66	4.45	5.90	20.74	5.13	64.46	9.67
3dNCF-900	90.47	4.08	5.38	17.75	4.19	66.07	11.98
3dNCF-1000	91.76	3.47	4.77	15.46	2.86	69.90	11.78

Table 3.2. Atomic content and nitrogen composition of 3dNC and 3dNCF-X calculated from the XPS survey spectra.

The optimized active site density and mass transport properties of the catalysts which facilitate the electrocatalytic performance are determined by such characteristics as high surface area, desired porous structure, and suitable chemical composition³⁰. So, 3dNCFs with tunable nitrogen contents and high surface area with micro/meso-pores can serve as promising alternatives for the ORR.

Cyclic voltammetry (CV) measurements were performed in 0.1 M KOH solution to examine the ORR catalytic activity of 3dNC and 3dNCF-Xs (CV). (Figure 3.10). As presented in CV curves, well-defined cathodic ORR peaks were observed in the CV analysis in the oxygen saturated solution while quasi-rectangular shapes without any distinct peak was detected for all of the catalysts in the nitrogen saturated solution, suggesting a pronounced oxygen catalytic activity. The distinct peak at around -0.23 V vs. the Ag/AgCl of 3dNCF-800 was comparable to that of Pt/C, and more positive than that of other samples (-0.29, -0.24 V, and -0.26 V for 3dNC, 3dNCF-900, and 3dNCF-1000, respectively, Figure 3.10), indicating the outstanding electrocatalytic performance of 3dNCF-800. Rotating disk electrode (RDE) measurement was further investigated to confirm the electrocatalytic performance of 3dNCFs. All the 3dNCF samples show outstanding electrocatalytic activity with a smaller ORR overpotential and a larger current density than that of 3dNC due to the abundant catalytic active sites exposed to electrochemical interface and superior mass transport of oxygen molecules. Also, 3dNCFs show well-defined one step ORR process compared to a two-step process for undoped-3dCF with a similar surface area and porosity, which emphasize the importance of selecting the suitable carbon precursors to fabricate electrocatalyst. Particularly, 3dNCF-800 exhibited the most positive onset potential (-0.15 V) and half wave potential ($E_{1/2}$) of -0.113 V, well comparable to the Pt/C catalyst and exceeds most previously fabricated metal-free catalysts^{31, 32, 7, 18, 33, 34, 13, 30} and carbon supported transition metal/nitrogen compounds^{35, 36, 37, 6, 5, 12} (Table 3.3). Linear sweep voltammetry (LSV) of 3dNCF-800 was measured at various disk rotating speeds (400 to 2500 rpm) in an O₂-purged 0.1 M potassium hydroxide solution (Figure 3.11 b). 3dNCF-800 exhibited a well-defined plateau of diffusion-limiting current below -0.2 V at all rotating speeds, demonstrating a direct four-electron transfer pathway with efficient electrocatalytic reaction. The electrochemical impedance spectroscopy measurements (Figure 3.12) confirm that the charge-transfer resistance of 3dNCF-800 was much lower than those of other 3dNCFs, demonstrating the better oxygen reduction kinetic property of 3dNCF-800 compared with others. Rotating ring-disk electrode (RRDE) measurements were conducted to investigate the ORR pathways of each sample. Based on the each current from the ring and disk, the H₂O₂ yield for 3dNCF-X was less than 7 % over the whole potential range and decreased to 0.68 % at 0.2 V, demonstrating a high electron transfer number ($n = 3.85 - 3.99$) similar to that of Pt/C (~ 4.0), which indicates that 3dNCF-800 favored a four electron ORR pathway. Kinetic currents derived from the mass transport correction of the ORR currents (figure 3.11 d) show a Tafel slope of 57 mV decade⁻¹ for 3dNCF-800 which is lower than that of Pt/C (68 mV decade⁻¹), demonstrating the superior ORR kinetics and activity

of 3dNCF-800³⁸. Although it is still controversial³⁹, the high ORR activity of nitrogen doped carbon nanomaterials usually contributed to the doped pyridinic N at the edge of graphitic carbon and the graphitic N in graphitic carbon layers by reducing the oxygen adsorption energy barrier on carbon atoms and accelerating of oxygen-oxygen bonds^{11, 37}. Also, it have been reported that the overall ORR property is mostly dependent on the relative proportion of graphitic N instead of total nitrogen contents¹³. The high electrocatalytic performance of 3dNCF-800 with a relatively low specific surface area (even though the overall surface area doesn't directly confirm the higher catalytic performance⁷) and low graphitic N proportion than other 3dNCFs is unclear and now under investigation.

One of the possible reason for the outstanding ORR performance of 3dNCF-800 is remained transition metal impurities which could increase the ORR catalytic activity^{40, 41}. Although the XPS measurements didn't reveal the iron species at all probably due to its limited analytic sensitivity, further investigation by employing inductively coupled plasma optical emission spectrometry (ICP-OES) confirmed the small amount of residual iron species(0.17 wt%) in 3dNCF-800. The remained Fe residue can offer efficient coordination with pyridinic N to form highly active ORR sites, which is partially proved by SCN⁻ probes⁴²(Figure 3.16). As the temperature increases above 900 °C, the Fe-N coordination starts to dissociate and hence decrease the ORR activity for 3dNCF-900 and 3dNCF-1000. In this regard, the prominent ORR performance in acidic media(Figure 3.11e) attributed to the synergistic effect of residual metal impurities which act as active center at acidic medium as well as the hierarchical porous architecture of the catalysts. The stability of 3dNCF-800 and Pt/C was investigated by using chronoamperometric (CA) measurement at a constant potential of -0.25 V in oxygen purged 0.1 M potassium hydroxide electrolyte with rotation speed of 1600 rpm. 3dNCF-800 maintained approximately 97 % current after over 20000 seconds of measurements, whereas Pt/C exhibited a large current loss hence presented 77 % current, which indicates the better stability of 3dNCF. Besides the remarkable long-term stability, 3dNCF-800 also exhibited excellent methanol cross over resistance, which suggests 3dNCF-800 could be the promising candidate for direct methanol alkaline fuel cells.

The bifunctional electrocatalytic activity of 3dNCF was investigated and compared to that of RuO₂ and Pt/C (Figure 3. 11f). 3dNCF-800 demonstrates good OER catalytic performances with its lower onset potentials and higher current density than that of Pt/C. Interestingly, 3dNCF-800 exhibited a lower onset potential than the commercial RuO₂ catalysts, which is contributed to its hierarchical porous structures with large density of pyridinic N active sites partially coordinated to Fe.

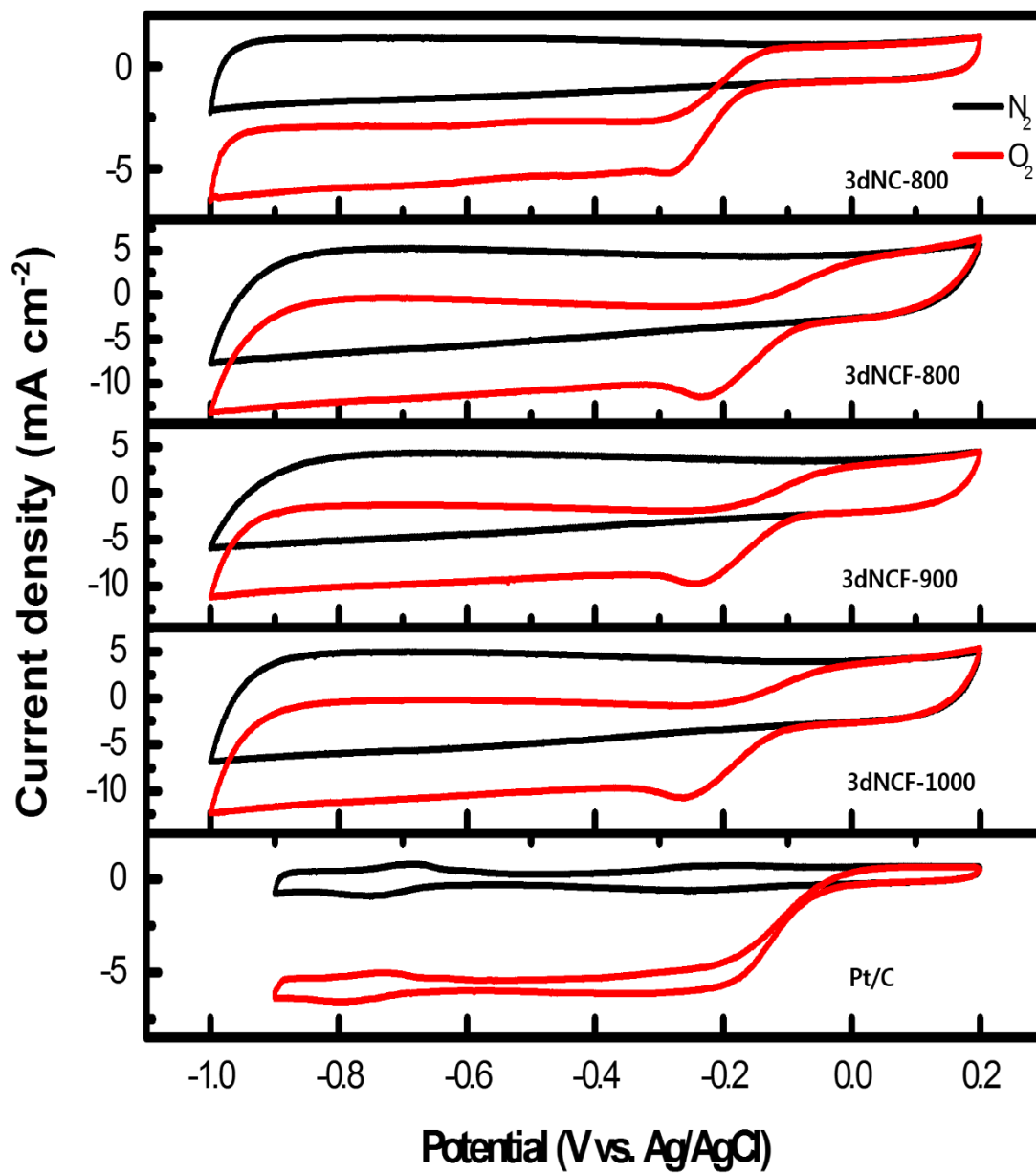


Figure. 3.10. Cyclic voltammety curves of the prepared catalysts and commercial Pt/C catalyst in 0.1 M KOH saturated with N₂ (Black curves) or O₂ (Red curves).

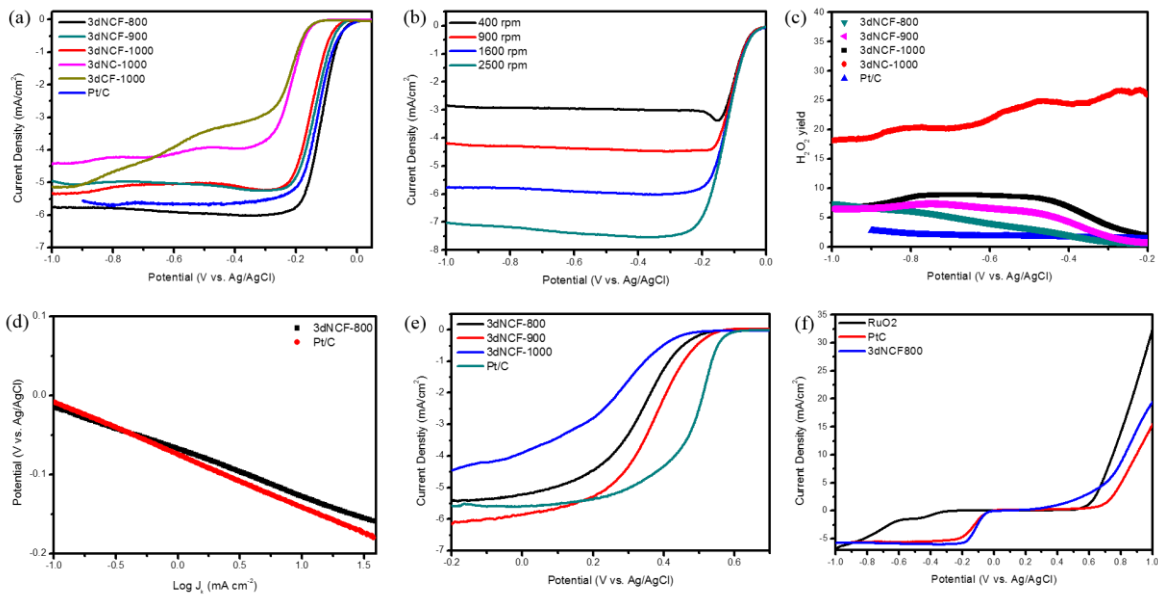


Figure 3.11 a) Linear sweep voltammetry (LSV) of 3dNC, 3dCF, and 3dNCF-X in oxygen-saturated 0.1 M KOH with a RDE rotation rate of 1600 rpm. b) LSV curves of 3dNCF-800 in oxygen-saturated 0.1 M KOH at various rotating speeds. c) H_2O_2 yields plots of 3dNC, 3dNCF-X, and Pt/C catalyst. d) Tafel plots measured in Oxygen-saturated 0.1M KOH. e) LSV curves for 3dNCF-X and Pt/C in 0.5 M H_2SO_4 for metal-free catalysts and 0.1 M HClO_4 for Pt/C. For all the RDE and the RRDE tests, the mass loading of catalysts was $20 \mu\text{g}_{\text{Pt}} \text{cm}^{-2}$ for Pt/C and 0.6 mg cm^{-2} for carbon catalysts. f) LSV curves of 3dNCF-800, RuO_2 and commercial Pt/C catalyst on an RDE in 0.1 M KOH with a RDE rotation speed 1600 rpm. All of the LSV scan rate is fixed at 10 mVs^{-1}

Catalysts	Loadings (mg cm ⁻²)	Half-wave Potential (V vs RHE)	References
N-doped ordered mesoporous Graphitic arrays	-	0.66	Angew. Chem. 2010, 122, 2619
N-doped macro/mesoporous carbon	-	0.82	Energy. Environ. Sci., 2015, 8, 3274
N-doped micro and mesoporous carbon	0.1	0.85	Nat. Commun. 2014, 5, 4973
N, P doped mesoporous carbon foam	0.15	0.85	Nat. Nanotech. 2015, 10, 444
P-doped ordered mesoporous carbon	-	-0.30(vs. Ag AgCl)	J. AM. Chem. Soc. 2012, 134, 16127
N, S co-doped carbon nanospheres	-	0.842 V vs RHE	Carbon, 2014, 69, 294
N-doped carbon nanosheets	0.6	0.84	Angew. Chem. Int. Ed. 2014, 53, 1570
N-doped mesoporous carbon	0.67	0.735	Angew. Chem. Int. Ed. 2015, 54, 588.

Catalysts	Loadings (mg cm ⁻²)	Half-wave Potential (V vs. RHE)	References
Fe-pC-Py-CNTs	0.32	0.915	Nat. Commun. 2013, 4, 2076
Fe-N-CNFs		-0.140 (vs. Ag AgCl) 0.81 V vs RHE.	Angew. Chem. 2015, 217, 8297
Co ₃ O ₄ /N-rmGO		0.83 (vs. RHE)	Nat. Mater. 2011, 10, 780
Fe ₃ C/C-800		0.83 (vs. RHE)	Angew. Chem. Int. Ed. 2014, 53, 3675
Fe@N-C-700	-	0.83	Nano Energy, 2015, 13, 387
CNT/(N/C)-800	0.5	0.848	Nanoscale, 2015, 7, 19201
Pt/C (Premetek)	0.1 (20ug _{pt} cm ⁻²)	0.84	This study
3dNCF-800	0.5	0.85	This study

Table 3.3. Comparison of ORR performance in 0.1 M KOH electrolyte of 3dNCF and with literature values.

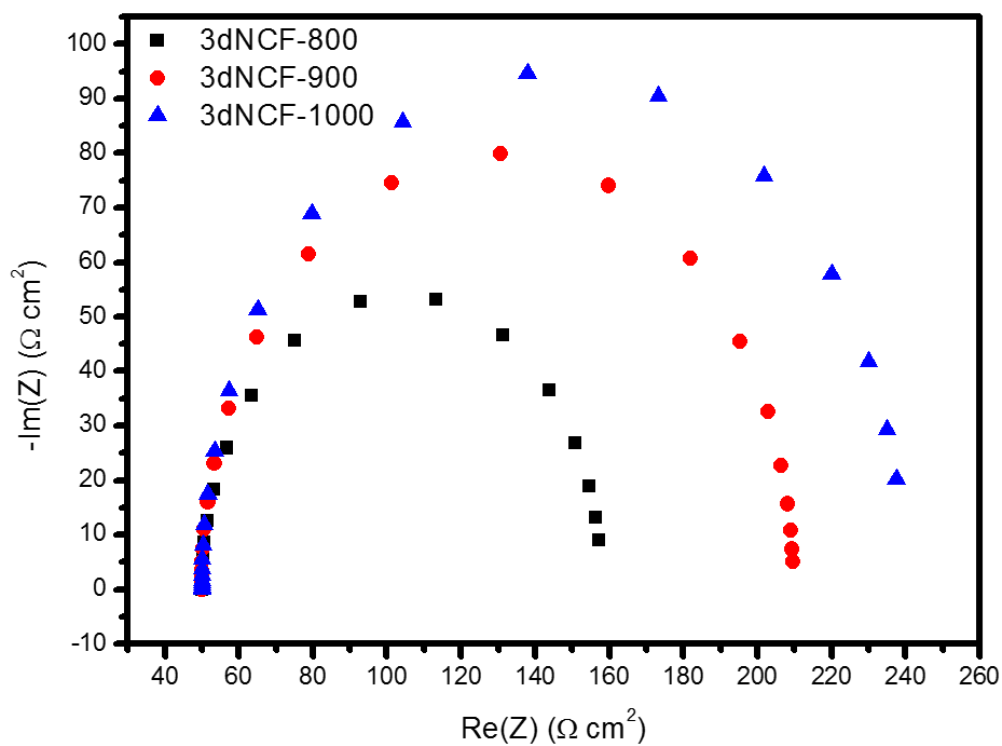


Figure 3.12 Electrochemical impedance spectroscopy (EIS) analysis of the catalysts. EIS were measured in O_2 -saturated 0.1 M KOH at -0.115 V vs. Ag/AgCl with 5 mV ac potential from 10 kHz to 0.01 Hz. The catalyst loading was 0.6 mg/cm^2 for all catalysts.

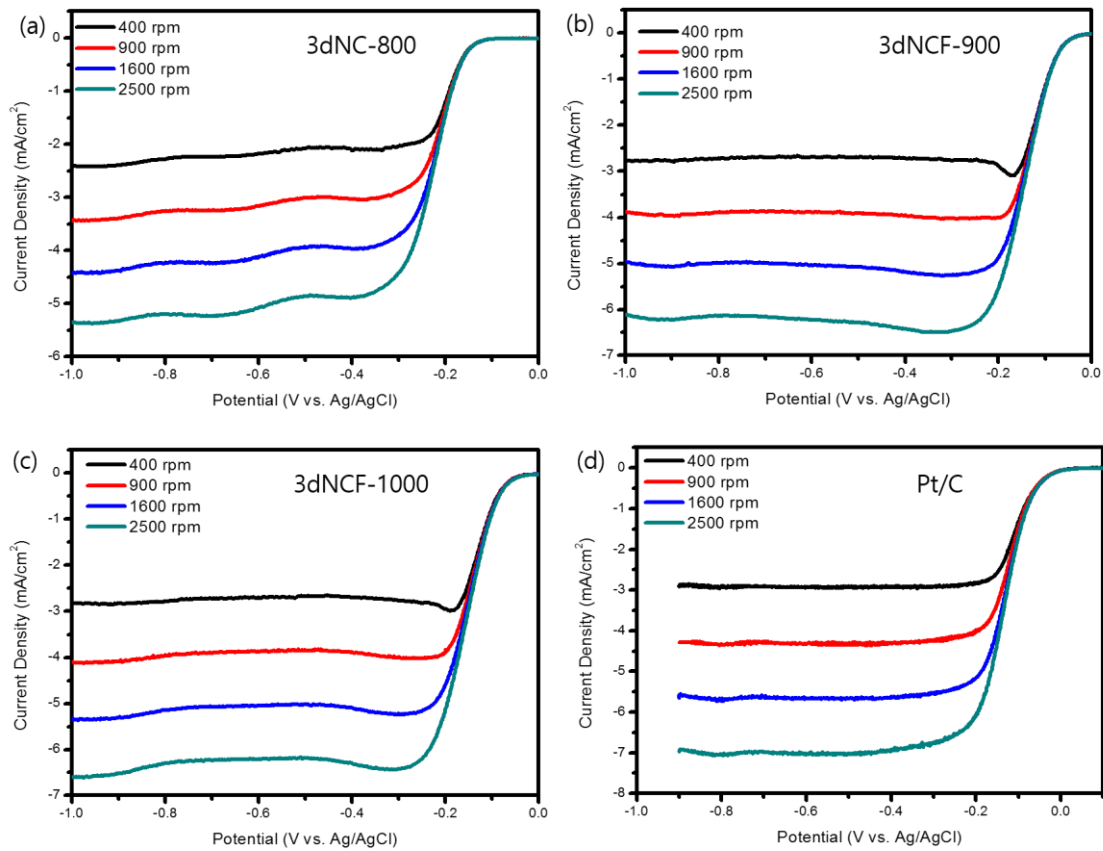


Figure. 3.13 LSV curves of 3dNC-800 (a), 3dNCF-900 (b), 3dNCF-1000 (c), Pt/C (d) in oxygen-saturated 0.1 M KOH with various rotating speeds.

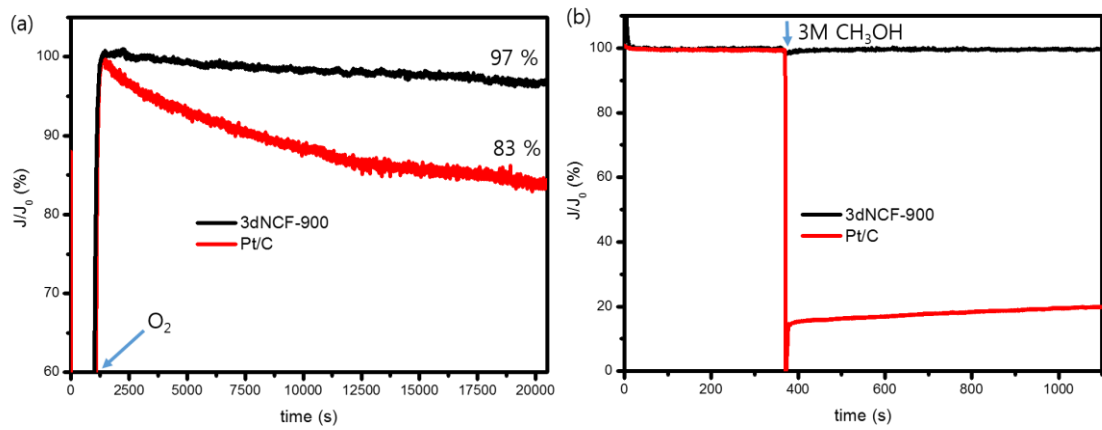


Figure. 3.14. Current-time (i-t) Chronoamperometric response (a) for 3dNCF-900 and Pt/C kept at -0.25 V versus Ag/AgCl in N_2 - and O_2 -saturated 0.1 M KOH electrolyte. The arrow indicates the O_2 injection. (b) The arrow indicates the addition of 3 M Methanol.

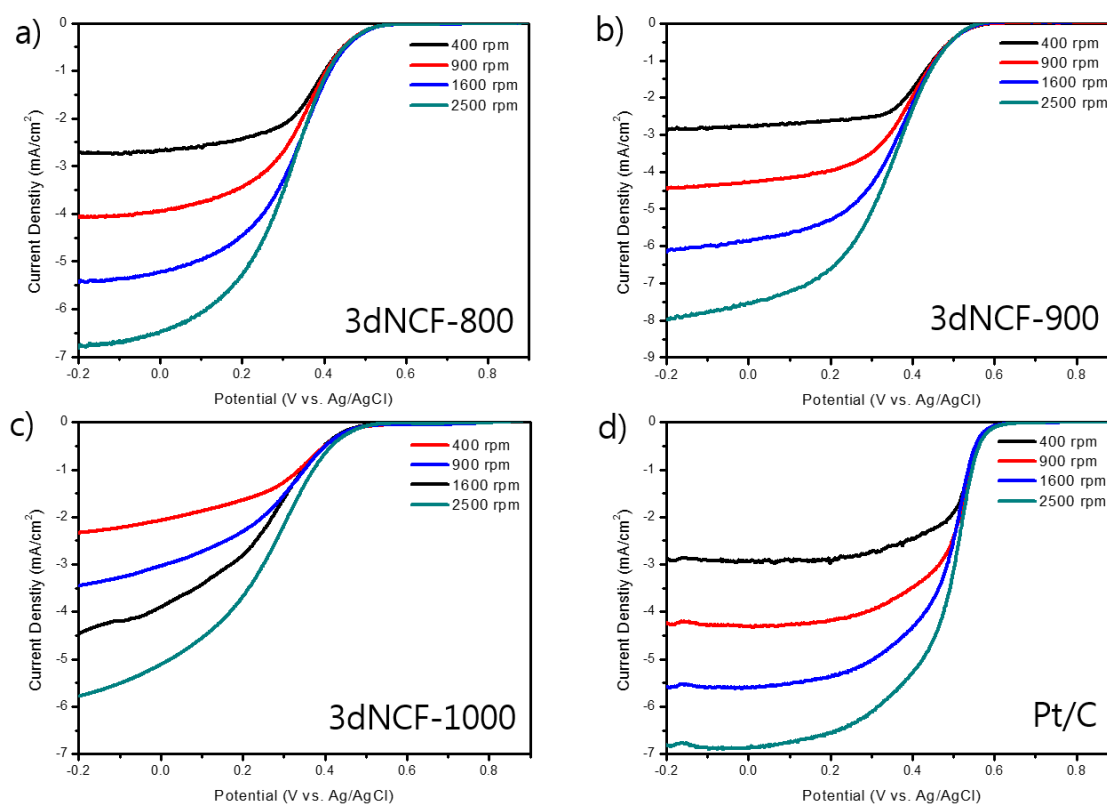


Figure. 3. 15. LSV curves of 3dNCF-800 (a), 3dNCF-900 (b), 3dNCF-1000 (c), Pt/C (d) in oxygen-saturated 0.5 M H₂SO₄ for metal-free catalysts and 0.1 M HClO₄ for Pt/C with various rotating speeds.

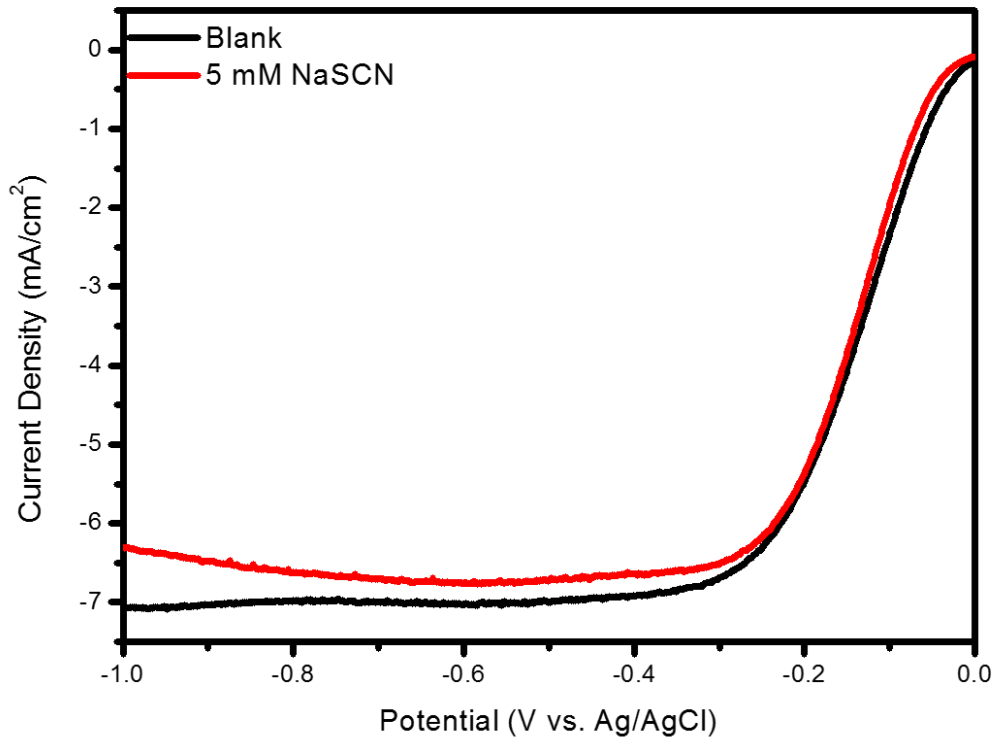


Figure 3. 16 Linear sweep voltammograms (LSV) of 3dNCF-800 on a rotating disk electrode at 1600 rpm in O₂ saturated 0.1 M KOH with and without NaSCN.

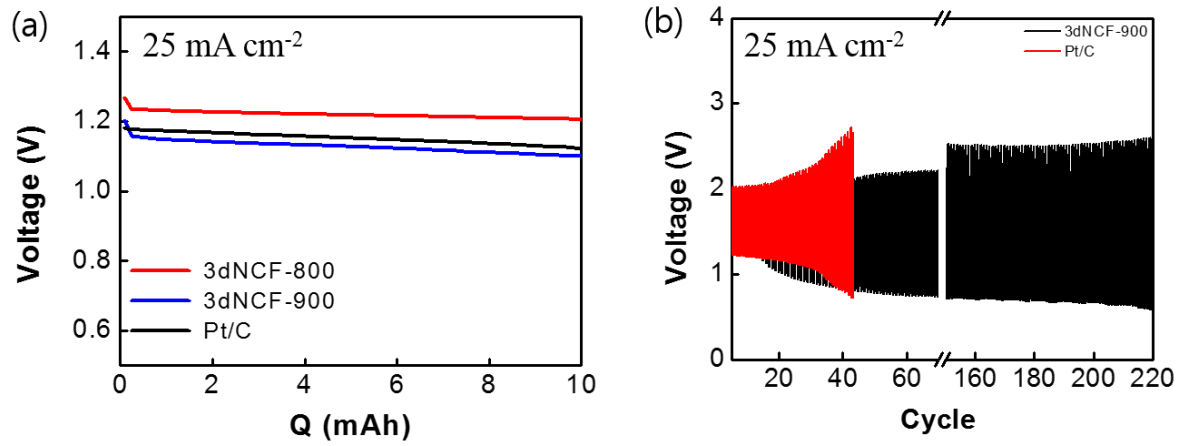


Figure 3.17. Two electrode Zn-air battery performance. Discharge curves of the Zn-air batteries using 3dNCF-800, 3dNCF-900 and Pt/C catalyst at 25 mA cm^{-2} (a). Discharge/charge cycling test at a current density of 25 mA cm^{-2} using the 3dNCF-900 and Pt/C as air electrodes.

The hierarchical porous structure and high density of active sites of 3dNCF which guarantee the remarkable electrocatalytic performance make it promising oxygen catalyst for Zn-air battery. To investigate the real device performance of 3dNCFs, two-electrode Zn-air cell is constructed by employing the 3dNCF as the air catalysts (cathode) and Zn plate as the anode. The cutting-edge Pt/C catalyst was also examined under the same condition. The zinc-air battery performances from 3dNCF-800 generates stable voltage of 1.23 V at 25 mA cm⁻² which is higher than that of Pt/C catalyst (1.18 V) demonstrating the good electrocatalytic performance of 3dNCF-800 in this device configuration. (Figure 3.17 a) Moreover, the prepared catalyst (3dNCF-900) shows good rechargeability confirmed by over 200 charge/discharge cycles at high current density (25 mA cm⁻²), which is better than that of Pt/C catalyst (Figure 3.17b). Even though further investigation is needed, these results suggest that 3dNCFs have great potential as promising electrocatalysts for Zn-air battery.

3.4. Conclusion.

We have fabricated three-dimensional hierarchical porous nitrogen doped carbon foams (3dNCF) with facile and scalable process by employing PVP, silica, and iron salts as a carbon source possessing nitrogen, sacrificial template, and graphitization agent, respectively. The resultant 3dNCFs exhibit efficient electrocatalytic activities for both ORR and OER as bifunctional air electrodes in Zn-air batteries. Especially, the Zn-air cell based on our 3dNCF air electrode operating in an aqueous KOH electrolyte exhibited 1.23 V at 25 mA cm⁻² which is higher than that of Pt/C air electrode based Zn-air cell. The desirable nitrogen contents and highly porous architectures of the 3dNCFs are essential for enhanced catalytic properties toward both ORR and OER.

3.4. References

1. Li, Y.; Dai, H., Recent advances in zinc-air batteries. *Chemical Society Reviews* **2014**, *43* (15), 5257-5275.
2. Cheng, F.; Chen, J., Metal-air batteries: from oxygen reduction electrochemistry to cathode catalysts. *Chemical Society Reviews* **2012**, *41* (6), 2172-2192.
3. Li, Y.; Gong, M.; Liang, Y.; Feng, J.; Kim, J.-E.; Wang, H.; Hong, G.; Zhang, B.; Dai, H., Advanced zinc-air batteries based on high-performance hybrid electrocatalysts. *Nature communications* **2013**, *4*, 1805.
4. Neburchilov, V.; Wang, H.; Martin, J. J.; Qu, W., A review on air cathodes for zinc-air fuel cells. *Journal of Power Sources* **2010**, *195* (5), 1271-1291.
5. Wang, J.; Wu, H.; Gao, D.; Miao, S.; Wang, G.; Bao, X., High-density iron nanoparticles encapsulated within nitrogen-doped carbon nanoshell as efficient oxygen electrocatalyst for zinc-air battery. *Nano Energy* **2015**, *13*, 387-396.
6. Hu, Y.; Jensen, J. O.; Zhang, W.; Cleemann, L. N.; Xing, W.; Bjerrum, N. J.; Li, Q., Hollow spheres of iron carbide nanoparticles encased in graphitic layers as oxygen reduction catalysts. *Angewandte Chemie* **2014**, *53* (14), 3675-9.
7. Liang, H. W.; Zhuang, X.; Bruller, S.; Feng, X.; Mullen, K., Hierarchically porous carbons with optimized nitrogen doping as highly active electrocatalysts for oxygen reduction. *Nature communications* **2014**, *5*, 4973.
8. Zhao, Y.; Nakamura, R.; Kamiya, K.; Nakanishi, S.; Hashimoto, K., Nitrogen-doped carbon nanomaterials as non-metal electrocatalysts for water oxidation. *Nature communications* **2013**, *4*, 2390.
9. Wang, S.; Iyyamperumal, E.; Roy, A.; Xue, Y.; Yu, D.; Dai, L., Vertically Aligned BCN Nanotubes as Efficient Metal-Free Electrocatalysts for the Oxygen Reduction Reaction: A Synergetic Effect by Co-Doping with Boron and Nitrogen. *Angewandte Chemie International Edition* **2011**, *50* (49), 11756-11760.
10. Liang, J.; Jiao, Y.; Jaroniec, M.; Qiao, S. Z., Sulfur and nitrogen dual-doped mesoporous graphene electrocatalyst for oxygen reduction with synergistically enhanced performance. *Angewandte Chemie International Edition* **2012**, *51* (46), 11496-11500.
11. Dai, L.; Xue, Y.; Qu, L.; Choi, H.-J.; Baek, J.-B., Metal-Free Catalysts for Oxygen Reduction Reaction. *Chemical reviews* **2015**.
12. Li, J. C.; Zhao, S. Y.; Hou, P. X.; Fang, R. P.; Liu, C.; Liang, J.; Luan, J.; Shan, X. Y.; Cheng, H. M., A nitrogen-doped mesoporous carbon containing an embedded network of carbon nanotubes as a highly efficient catalyst for the oxygen reduction reaction. *Nanoscale* **2015**, *7* (45), 19201-6.
13. Wei, W.; Liang, H.; Parvez, K.; Zhuang, X.; Feng, X.; Mullen, K., Nitrogen-doped carbon nanosheets with size-defined mesopores as highly efficient metal-free catalyst for the oxygen reduction

reaction. *Angewandte Chemie* **2014**, *53* (6), 1570-4.

14. Wang, X.; Lee, J. S.; Zhu, Q.; Liu, J.; Wang, Y.; Dai, S., Ammonia-treated ordered mesoporous carbons as catalytic materials for oxygen reduction reaction. *Chemistry of Materials* **2010**, *22* (7), 2178-2180.

15. Wei, Z.; Ding, W.; Wan, L.-J. In *Space-Confinement-Induced Synthesis of Planar Nitrogen-Doped Graphene for Catalysis of Oxygen Reduction*, 2014 Electrochemical Conference on Energy & the Environment (ECEE-March 13-16, 2014), Ecs: 2014.

16. Proietti, E.; Jaouen, F.; Lefèvre, M.; Larouche, N.; Tian, J.; Herranz, J.; Dodelet, J.-P., Iron-based cathode catalyst with enhanced power density in polymer electrolyte membrane fuel cells. *Nature communications* **2011**, *2*, 416.

17. Liang, J.; Zheng, Y.; Chen, J.; Liu, J.; Hulicova-Jurcakova, D.; Jaroniec, M.; Qiao, S. Z., Facile Oxygen Reduction on a Three-Dimensionally Ordered Macroporous Graphitic C₃N₄/Carbon Composite Electrocatalyst. *Angewandte Chemie International Edition* **2012**, *51* (16), 3892-3896.

18. Zhang, J.; Zhao, Z.; Xia, Z.; Dai, L., A metal-free bifunctional electrocatalyst for oxygen reduction and oxygen evolution reactions. *Nature nanotechnology* **2015**, *10* (5), 444-52.

19. Wu, G.; More, K. L.; Johnston, C. M.; Zelenay, P., High-performance electrocatalysts for oxygen reduction derived from polyaniline, iron, and cobalt. *Science* **2011**, *332* (6028), 443-447.

20. Hou, J.; Cao, C.; Idrees, F.; Ma, X., Hierarchical Porous Nitrogen-Doped Carbon Nanosheets Derived from Silk for Ultrahigh-Capacity Battery Anodes and Supercapacitors. *ACS nano* **2015**, *9* (3), 2556-2564.

21. Yoon, J.-C.; Lee, J.-S.; Kim, S.-I.; Kim, K.-H.; Jang, J.-H., Three-dimensional graphene nano-networks with high quality and mass production capability via precursor-assisted chemical vapor deposition. *Scientific reports* **2013**, *3*.

22. Garsany, Y.; Singer, I. L.; Swider-Lyons, K. E., Impact of film drying procedures on RDE characterization of Pt/VC electrocatalysts. *Journal of Electroanalytical Chemistry* **2011**, *662* (2), 396-406.

23. Chen, Z.; Higgins, D.; Chen, Z., Electrocatalytic activity of nitrogen doped carbon nanotubes with different morphologies for oxygen reduction reaction. *Electrochimica Acta* **2010**, *55* (16), 4799-4804.

24. Ferrari, A.; Meyer, J.; Scardaci, V.; Casiraghi, C.; Lazzeri, M.; Mauri, F.; Piscanec, S.; Jiang, D.; Novoselov, K.; Roth, S., Raman spectrum of graphene and graphene layers. *Physical review letters* **2006**, *97* (18), 187401.

25. Ferrari, A. C.; Robertson, J., Interpretation of Raman spectra of disordered and amorphous carbon. *Physical review B* **2000**, *61* (20), 14095.

26. Huang, X.; Qian, K.; Yang, J.; Zhang, J.; Li, L.; Yu, C.; Zhao, D., Functional nanoporous graphene foams with controlled pore sizes. *Advanced materials* **2012**, *24* (32), 4419-23.

27. Du, Y. K.; Yang, P.; Mou, Z. G.; Hua, N. P.; Jiang, L., Thermal decomposition behaviors of PVP coated on platinum nanoparticles. *Journal of Applied Polymer Science* **2006**, *99* (1), 23-26.
28. Chen, S.; Bi, J.; Zhao, Y.; Yang, L.; Zhang, C.; Ma, Y.; Wu, Q.; Wang, X.; Hu, Z., Nitrogen-Doped Carbon Nanocages as Efficient Metal-Free Electrocatalysts for Oxygen Reduction Reaction. *Advanced materials* **2012**, *24* (41), 5593-5597.
29. Shin, D.; Jeong, B.; Mun, B. S.; Jeon, H.; Shin, H.-J.; Baik, J.; Lee, J., On the Origin of Electrocatalytic Oxygen Reduction Reaction on Electrospun Nitrogen–Carbon Species. *The Journal of Physical Chemistry C* **2013**, *117* (22), 11619-11624.
30. Wang, G.; Sun, Y.; Li, D.; Liang, H. W.; Dong, R.; Feng, X.; Mullen, K., Controlled Synthesis of N-Doped Carbon Nanospheres with Tailored Mesopores through Self-Assembly of Colloidal Silica. *Angewandte Chemie* **2015**.
31. Liu, R.; Wu, D.; Feng, X.; Müllen, K., Nitrogen-doped ordered mesoporous graphitic arrays with high electrocatalytic activity for oxygen reduction. *Angewandte Chemie* **2010**, *122* (14), 2619-2623.
32. Li, L.; Liu, C.; He, G.; Fan, D.; Manthiram, A., Hierarchical pore-in-pore and wire-in-wire catalysts for rechargeable Zn– and Li–air batteries with ultra-long cycle life and high cell efficiency. *Energy Environ. Sci.* **2015**, *8* (11), 3274-3282.
33. Yang, D.-S.; Bhattacharjya, D.; Inamdar, S.; Park, J.; Yu, J.-S., Phosphorus-doped ordered mesoporous carbons with different lengths as efficient metal-free electrocatalysts for oxygen reduction reaction in alkaline media. *Journal of the American Chemical Society* **2012**, *134* (39), 16127-16130.
34. You, C.; Liao, S.; Li, H.; Hou, S.; Peng, H.; Zeng, X.; Liu, F.; Zheng, R.; Fu, Z.; Li, Y., Uniform nitrogen and sulfur co-doped carbon nanospheres as catalysts for the oxygen reduction reaction. *Carbon* **2014**, *69*, 294-301.
35. Cao, R.; Thapa, R.; Kim, H.; Xu, X.; Kim, M. G.; Li, Q.; Park, N.; Liu, M.; Cho, J., Promotion of oxygen reduction by a bio-inspired tethered iron phthalocyanine carbon nanotube-based catalyst. *Nature communications* **2013**, *4*.
36. Wu, Z. Y.; Xu, X. X.; Hu, B. C.; Liang, H. W.; Lin, Y.; Chen, L. F.; Yu, S. H., Iron Carbide Nanoparticles Encapsulated in Mesoporous Fe-N-Doped Carbon Nanofibers for Efficient Electrocatalysis. *Angewandte Chemie* **2015**, *54* (28), 8179-83.
37. Liang, Y.; Li, Y.; Wang, H.; Zhou, J.; Wang, J.; Regier, T.; Dai, H., Co₃O₄ nanocrystals on graphene as a synergistic catalyst for oxygen reduction reaction. *Nature materials* **2011**, *10* (10), 780-786.
38. Choi, H.-J.; Kumar, N. A.; Baek, J.-B., Graphene supported non-precious metal-macrocycle catalysts for oxygen reduction reaction in fuel cells. *Nanoscale* **2015**, *7* (16), 6991-6998.
39. Wei, Q.; Tong, X.; Zhang, G.; Qiao, J.; Gong, Q.; Sun, S., Nitrogen-Doped Carbon Nanotube and Graphene Materials for Oxygen Reduction Reactions. *Catalysts* **2015**, *5* (3), 1574-1602.

40. Wang, L.; Ambrosi, A.; Pumera, M., “Metal-Free” Catalytic Oxygen Reduction Reaction on Heteroatom-Doped Graphene is Caused by Trace Metal Impurities. *Angewandte Chemie International Edition* **2013**, *52* (51), 13818-13821.
41. Liu, J.; Sun, X.; Song, P.; Zhang, Y.; Xing, W.; Xu, W., High-Performance Oxygen Reduction Electrocatalysts based on Cheap Carbon Black, Nitrogen, and Trace Iron. *Advanced materials* **2013**, *25* (47), 6879-6883.
42. Zhou, X.; Bai, Z.; Wu, M.; Qiao, J.; Chen, Z., 3-Dimensional porous N-doped graphene foam as a non-precious catalyst for the oxygen reduction reaction. *Journal of Materials Chemistry A* **2015**, *3* (7), 3343-3350.